Title

Acute pharmacological inhibition of matrix metalloproteinase-9 activity during development restores perineuronal net formation and normalizes auditory processing in Fmr1 KO mice

Journal

Journal of Neurochemistry, 155(5)

ISSN

0022-3042

Authors

Pirbhoy, Patricia S
Rais, Maham
Lovelace, Jonathan W
et al.

Publication Date

2020-12-01

DOI

10.1111/jnc.15037

Peer reviewed

Article Type: Original Article

Acute pharmacological inhibition of matrix metalloproteinase-9 activity during development restores perineuronal net formation and normalizes auditory processing in *Fmr1* KO mice

Patricia S. Pirbhoy[1], Maham Rais[1], Jonathan W. Lovelace[2], Walker Woodard[1], Khaleel A. Razak[2], Devin K. Binder[1], Iryna M. Ethell[1] (*)

[1] Division of Biomedical Sciences, School of Medicine, University of California, Riverside Riverside, California 92521, USA

[2] Department of Psychology, University of California Riverside, Riverside, California 92521, USA

*Corresponding author: Iryna M. Ethell, Ph.D.

Division of Biomedical Sciences, School of Medicine,

University of California, Riverside

Riverside, California 92521, USA

Tel: (951)-827-2186

Email: iryna.ethell@medsch.ucr.edu

Orchid ID: 0000-0002-1324-6611

Running Title (45 characters): MMP9 inhibition attenuates auditory deficits in FXS

Key words

Fragile X Syndrome

Electroencephalography

Matrix Metalloproteinase-9

Sensory Hypersensitivity

Perineuronal Nets

Parvalbumin

Abbreviations:

AC, Auditory Cortex

Akt, Protein Kinase B

ASD, Autism Spectrum Disorders

EEG, Electroencephalography

FFT, Fast Fourier Transform

Fmr1 KO, *Fragile X mental retardation 1* gene knock-out

FXS, Fragile X Syndrome

FC, Frontal Cortex

ITPC, Inter trial phase coherence

mTOR, Mammalian target of rapamycin

MMP-2/9, Matrix metalloproteinase-2/9

PV, Parvalbumin

PNN, Perineuronal net

RRID, Research resource identifier

STP, Single trial power

TrkB, Tropomyosin-related kinase B

Total number of words: 7,840 (excluding Methods and References)

Abstract: 250

Introduction: 734

Results: 3413

Discussion: 2010

Figure legends: 1433

Abstract

Individuals with Fragile X Syndrome (FXS) and autism spectrum disorder (ASD) exhibit cognitive impairments, social deficits, increased anxiety, and sensory hyperexcitability. Previously, we showed that elevated levels of matrix metalloproteinase-9 (MMP-9) may contribute to abnormal development of parvalbumin (PV) interneurons and perineuronal nets (PNNs) in the developing auditory cortex (AC) of *Fmr1* knock-out (KO) mice, which likely underlie auditory hypersensitivity. Thus, MMP-9 may serve as a potential target for treatment of auditory hypersensitivity in FXS. Here, we used the MMP-2/9 inhibitor, SB-3CT, to pharmacologically inhibit MMP-9 activity during a specific developmental period and to test if inhibition of MMP-9 activity reverses neural oscillation deficits and behavioral impairments by enhancing PNN formation around PV cells in *Fmr1* KO mice. Electroencephalography (EEG) was used to measure resting state and sound-evoked electrocortical activity in auditory and frontal cortices of postnatal day (P)22-23 male mice before and one-day after treatment with SB-3CT (25 mg/kg) or vehicle. At P27-28, animal behaviors were tested to measure the effects of the treatment on anxiety and hyperactivity. Results show that acute inhibition of MMP-9 activity improved evoked synchronization to auditory stimuli, and ameliorated mouse behavioral deficits. MMP-9 inhibition enhanced PNN formation, increased PV levels and TrkB phosphorylation yet reduced Akt phosphorylation in the AC of *Fmr1* KO mice. Our results show that MMP-9

inhibition during early postnatal development is beneficial in reducing some auditory processing deficits in the FXS mouse model and may serve as a candidate therapeutic for reversing sensory hypersensitivity in FXS and possibly other ASDs.

Introduction

Fragile X Syndrome (FXS) is a neurodevelopmental disorder caused by the hypermethylation of the *Fragile X mental retardation 1 (Fmr1)* gene, resulting in the loss of the Fragile X Mental Retardation Protein (FMRP) (Verkerk *et al.* 1991), a regulator of protein synthesis (Laggerbauer 2001). FXS is the most prevalent cause of inherited intellectual disability (Hagerman *et al.* 2008) and a leading genetic cause of autism, providing a genetic model to study the neurobiological mechanisms underlying autism spectrum disorders (ASD) (Crawford *et al.* 2001; Hagerman *et al.* 2008). Individuals with FXS exhibit cognitive dysfunctions (Freund & Reiss 1991), increased anxiety (Talisa *et al.* 2014), and sensory hyperexcitability (Miller *et al.* 1999; Rotschafer & Razak 2013; Ethridge *et al.* 2016).

Auditory hypersensitivity in individuals with FXS and *Fmr1* knock-out (KO) mice is commonly characterized by a heightened response to non-aversive stimuli (Crane *et al.* 2009; McDiarmid *et al.* 2017; Sinclair *et al.* 2017; Rais *et al.* 2018), reduced ability to habituate to sounds (Castren *et al.* 2003; Ethridge *et al.* 2016; Lovelace *et al.* 2016; Wang *et al.* 2017), and greater resting state gamma power in electroencephalography (EEG) recordings (Ethridge *et al.* 2017; Wang *et al.* 2017; Lovelace *et al.* 2018; Lovelace *et al.* 2019). Studies in the *Fmr1* KO mice also show increased sensory responses, broader receptive fields, impaired sound selectivity (Rotschafer & Razak 2013) and abnormal network synchronization (Paluszkiewicz *et al.* 2011). It is hypothesized that the inability to habituate to auditory stimuli (Castren *et al.* 2003; Ethridge

et al. 2016) including ongoing background noise, a phenotype that is also observed in *Fmr1* KO mice (Lovelace *et al.* 2016; Lovelace *et al.* 2018), may contribute to hypersensitivity to sounds and cortical hyperexcitability (Gibson *et al.* 2008; Ethridge *et al.* 2016; Ethridge *et al.* 2017; Lovelace *et al.* 2018; Lovelace *et al.* 2019). Notably, EEG gamma frequency band abnormalities are associated with heightened sensory sensitivities and social communication deficits in FXS individuals (Ethridge *et al.* 2016; Ethridge *et al.* 2017; Ethridge *et al.* 2019). Taking advantage of the link between EEG abnormalities and sensory hypersensitivity in FXS, this study used these EEG measures to test the efficacy of a candidate treatment in *Fmr1* KO mice.

Individuals with FXS (Dziembowska *et al.* 2013) and *Fmr1* KO mice (Bilousova *et al.* 2009; Gkogkas *et al.* 2014; Sidhu *et al.* 2014) exhibit increased levels of the secreted endopeptidase, matrix metalloproteinase-9 (MMP-9). Specifically, *Fmr1* KO mice show elevated levels of MMP-9 in the auditory cortex (AC) during postnatal day (P) 3–18 period. It is hypothesized that increased activity of MMP-9 may contribute to the development of auditory hypersensitivity by excessively degrading PNNs thereby resulting in impaired PNN formation around PV interneurons and affecting PV development in the AC of *Fmr1* KO mice at P21 (Wen *et al.* 2018). Indeed, genetic reduction of MMP-9 levels enhanced PNN formation around PV interneurons and restored sound-evoked responses and spontaneous activity to WT levels (Wen *et al.* 2018). Genetic removal of MMP-9 also rescued altered event-related potential (ERP) habituation responses in the AC of adult *Fmr1* KO mice (Lovelace *et al.* 2016), normalized dendritic spine abnormalities in the hippocampus and improved abnormal behaviors in *Fmr1* KO mice (Sidhu *et al.* 2014). PV interneuron dysfunction contributes to abnormal network synchrony and alterations in gamma oscillations (Vreugdenhil *et al.* 2003; Lewis *et al.* 2005; Sohal *et al.* 2009). Overall these studies indicate that (1) MMP-9 may influence the development of

hypersensitive networks during the third and fourth postnatal weeks, a time that coincides with a critical developmental window for inhibitory and excitatory circuit maturation (Gibson *et al.* 2008; Oswald & Reyes 2008) and (2) that targeted inhibition of MMP-9 may serve as a candidate therapeutic to reduce auditory hypersensitivity in FXS.

In this study, we tested the hypothesis that acute pharmacological inhibition of aberrant MMP-9 activity during the critical developmental period would ameliorate cortical processing deficits, including abnormal resting state neural oscillatory patterns, the ability to synchronize to stimulus-induced oscillations, PV/PNN deficits, and behavioral impairments. Our results show that acute inhibition of MMP-9 during the P22-23 developmental period improved evoked synchronization to auditory stimuli and enhanced PNN formation around PV cells. We also observed beneficial effects of acute MMP-9 inhibition at P27-28 on animal behaviors, such as anxiety and hyperactivity. MMP-9 inhibition at P27-28 also increased PV levels and TrkB phosphorylation, and reduced aberrant Akt phosphorylation in the developing AC of *Fmr1* KO mice.

Materials and Methods

Ethics Statement

All experiments and animal care/use protocols were approved by the Institutional Animal Care and Use Committee at the University of California, Riverside (approval number 20190015 and 20190029) and were carried out in accordance with NIH "Guide for the Care and Use of Laboratory Animals." The study was not pre-registered.

Animals

Experimental animals were C57BL/6 mice obtained from Jackson Laboratories (RRID: IMSR_JAX:003025). Age-matched WT and *Fmr1* KO male mice were used between postnatal

day (P) 18-19 (EEG surgery N=79, N=14 died post-surgery), P22-23 [EEG recording (N=65) and PV/PNN analysis (N=24: note the same EEG animals were used for analysis) and DQ gelatin assay (N=16)] and P27-29 for behavior (N=37) and Western blot (N=8). For a detailed description of total animals and animals per group please refer to Figure 1, Figure 6, and Figure 7. A total of 140 male mice were used in this study with an average weight of 8 g and range from 6-18 g. All genotypes were confirmed with the analysis of tail samples by Transnetyx (Cordova, TN, USA), using real-time PCR-based system to probe for WT (fmr+/+forward: 5'-TGT GAT AGA ATA TGC AGC ATG TGA-3') or KO (fmr-/-forward: 5'CAC GAG ACT AGT GAG ACG TG-3') target sequence in each sample. Mice were maintained in an AAALAC accredited facility in 12 h light/dark cycles and food and water was available *ad libitum*. All experimental procedures were performed on C57BL/6 wild type (WT, RRID:IMSR_JAX:000664) and *Fragile X mental retardation gene-1 (Fmr1)* knock out (KO) mice (RRID: IMSR_JAX:003025, The Jackson Laboratory).

Surgery for electroencephalography recordings

Surgical procedures were performed as described in detail previously (Lovelace *et al.* 2018; Lovelace *et al.* 2019). Briefly, mice were anesthetized with isoflurane inhalation (0.2-0.5%) and given an intraperitoneal (i.p.) injection of ketamine and xylazine (K/X: 100/20 mg/kg). Toe pinch reflex was used to measure anesthetic state every 10 min throughout the surgery, and supplemental doses, no more than half of the original dose of K/X, were administered as needed. Mice were placed in a stereotaxic frame (model 930; Kopf, CA). Artificial tear gel was applied to the eyes to prevent drying. Once the mouse was anesthetized, a midline sagittal incision was made along the scalp to expose the skull. A Foredom dental drill was used to drill three holes 1mm in diameter in the skull overlying the right AC (-1.6mm,

+4.8mm), right frontal lobe (+2.6mm, +1.0mm), and left occipital cortex (-3.5mm, -5.2mm) (coordinate relative to bregma: anterior/posterior, medial/lateral). Three channel electrode posts (Plastics One, MS333-2-A-SPC) were attached to 1-mm stainless steel screws (Plastics One, 8L003905201F) and screws were advanced into the drilled holes until secure. Special care was taken not to advance the screws beyond the point of contact with the dura. Dental cement was applied around the screws, on the base of the post, and exposed skull. Postoperative care included topical application of a triple antibiotic ointment along the edges of the dental cement followed by two subcutaneous injections of buprenorphine (0.05 mg/kg), one immediately after surgery and one 6-10h after surgery. Mice were placed on a heating pad to aid recovery from anesthesia. Mice were group housed, returned to the vivarium and monitored daily until the day of EEG recordings, which allowed 4-5 days recovery post-surgery before recording.

Electrophysiology

All EEG recordings were performed during the hours of 5 AM to 7 PM. Mice were habituated for 20 min in an anechoic foam-lined sound-attenuating chamber (Gretch-Ken Industries Inc.) and connected to the BioPac acquisition system (BIOPAC Systems, Inc) through a 3-channel tether under brief isoflurane anesthesia. The tether was connected to a commutator located directly above the cage. Mice were then allowed to habituate to being connected to the tether for an additional 15 min before EEG recordings were obtained. During the recording session, a piezoelectric sensor placed under the floor of the cage detected mouse movement in the recording arena.

EEG activity was obtained using the BioPac system and Acqknowledge recording software from awake and freely moving mice. The BioPac MP150 acquisition system was connected to two EEG 100C amplifier units (one for each channel) to which the commutator was

attached. The lead to the occipital cortex served as a reference for both frontal and auditory cortex screw electrodes. The acquisition hardware was set to high-pass (>0.5 Hz) and low-pass (<100 Hz) filters. Normal EEG output data were collected with gain maintained the same (10,000 X) between all recordings. Data were sampled at a rate of 2.5 kHz using Acqknowledge software and down sampled to 1024 Hz post hoc using Analyzer 2.1 (Brain Vision LLC). Sound delivery was synchronized with EEG recording using a TTL pulse to mark the onset of each sound in a train. Resting EEGs were recorded for five minutes (during this time no auditory stimuli were presented) followed by recordings in response to auditory stimulation. After all EEG experiments were completed, mice were perfused for histology or used for behavioral tasks and Western blot analysis.

Acoustic stimulation

Acoustic stimulation paradigms were similar as those previously used in *Fmr1* KO mice (Lovelace *et al.* 2018; Lovelace *et al.* 2019), which is analogous to work in humans with FXS. Acoustic stimuli were generated using RPvdsEx software and RZ6 hardware (Tucker-Davis Technologies, FL) and presented through a free-field speaker (MF1 Multi-Field Magnetic Speaker; Tucker-Davis Technologies, FL) located 30 cm away directly above the cage. Sound pressure level (SPL) was modified using programmable attenuators in the RZ6 system. The speaker output was ~70 dB SPL at the floor of recording chamber with fluctuation of +/- 3 dB for frequencies between 5 and 35 kHz as measured with a ¼ in Bruel and Kjaer microphone.

A chirp-modulated signal (henceforth 'chirp') to induce synchronized oscillations in EEG recordings was used to quantify fidelity of responses to time varying stimuli. The chirp is a two-second broadband noise stimulus with amplitude modulated (100% modulation depth) by a sinusoid whose frequencies increase (Up-chirp) or decrease (Down-chirp) linearly in the 1-100

Hz range (Artieda *et al.* 2004; Perez-Alcazar *et al.* 2008; Purcell *et al.* 2004). The chirp facilitates a rapid measurement of transient oscillatory response (delta to gamma frequency range) to auditory stimuli of varying frequencies and can be used to compare oscillatory response in different groups in clinical and pre-clinical settings. Inter-trial phase coherence analysis (phase locking factor) can then be used to determine the ability of the neural generator to synchronize oscillations to the frequencies present in the stimulus (Tallon-Baudry *et al.* 1996). The chirp stimulus may be preferable over the traditional steady state stimulus in studies of children with neurodevelopmental disorders, as it can quickly and efficiently measure multiple modulation frequencies in a shorter period of time.

To avoid onset responses contaminating phase locking to the amplitude modulation of the chirp, the stimulus was ramped in sound level from 0 to 100% over 1 sec (rise time), which then smoothly transitioned into chirp modulation of the noise (see Figure 3C for example). Up and Down chirp trains were presented 300 times each (for a total of 600 trains). Both directions of modulation were tested to ensure any frequency-specific effects were not due to the frequency transition history within the stimulus. Up and Down trains were presented in an alternating sequence. The interval between each train was randomly varied between 1 and 1.5 s.

Data Analysis

All EEG data analysis was performed as described previously (Lovelace *et al.* 2019; Lovelace *et al.* 2018). Briefly, EEG data was extracted from Acqknowledge and converted to files compatible with Analyzer 2.1 software. All data were notched filtered at 60 Hz to remove residual line noise from recordings. Artifact rejection was performed using BrainVision Analyzer. Several criteria were used to search for artifacts including amplitude, gradient, max-min and low activity. Less than 30% of data were rejected due to artifacts from any single

mouse. If more than 30% of the data was rejected, the animal was excluded from analysis (Resting baseline: WT PRE, N=1; *Fmr1* KO PRE, N=1; vehicle-treated *Fmr1* KO, N=2; vehicle-treated WT, N=2; SB-3CT-treated *Fmr1* KO, N=1; Chirp: *Fmr1* KO PRE, N=2, vehicle-treated WT, N=1; SB-3CT-treated WT,N=1; *Fmr1* KO, N=2, SB-3CT-treated *Fmr1* KO, N=1). Notably, no outlier test was performed; instead, animals were excluded based on the exclusion criterion described above or movement percentage.

Resting EEG analysis

Five minutes of EEG data (no auditory stimulus) were divided into 2-sec segments and Fast Fourier Transforms (FFT) were calculated on each segment using 0.5 Hz bins, using a Hanning window, with no overlap, and then average power (μV^2/Hz) was calculated for each mouse from 1 to 100 Hz. Power was then further binned into standard frequency bands: We compared genotype mean differences on 6 bands per region: Delta (1-4 Hz), Theta (4-8 Hz), Alpha (8-13 Hz), Beta (13-30 Hz), Low Gamma (30-55 Hz), and High Gamma (65-100 Hz). The gamma band (30-100 Hz) was divided into low (30-60 Hz) versus high (>60 Hz) bands in gamma range because studies show the lower gamma frequency rhythm may be associated with activity of PV cells (Ray & Maunsell 2011; Balakrishnan & Pearce 2014; Dvorak & Fenton 2014), while the higher gamma frequencies may be related to spiking activity near the electrodes (Ray & Maunsell 2011; Buzsaki & Wang 2012). The spectral bands used are based on a number of previous studies on FXS in both mice (Radwan *et al.* 2016) and humans (Ethridge *et al.* 2017; Wang *et al.* 2017; Ethridge *et al.* 2016).

Responses to chirp trains were analyzed using Morlet wavelet analysis. Chirp trains were segmented into windows of 500ms before chirp onset to 500ms after the end of the chirp sound (total of 3 sec because each chirp was 2 s in duration). EEG traces were processed with Morlet

wavelets from 1 to 100 Hz using complex number output (voltage density, μV/Hz) for Inter Trial Phase Coherence (ITPC) calculations, and power density (μV^2/Hz) for non-phase locked single trial power (STP). Wavelets were run with a Morlet parameter of 10 as this gave the best frequency/power discrimination. This parameter was chosen since studies in humans found most robust difference around 40 Hz, where this parameter is centered (Ethridge *et al.* 2017). To measure phase synchronization at each frequency across trials, Inter Trial Phase Coherence (ITPC) was calculated. The equation used to calculate ITPC is:

$$ITPC(f,t) = \frac{1}{n}\sum_{k=1}^{n}\frac{F_k(f,t)}{|F_k(f,t)|}$$

where f is the frequency, t is the time point, and κ is the trial number. Thus, $F_k(f,t)$ refers to the complex wavelet coefficient at a given frequency and time for the κth trial. There were no less than 225 trials (out of 300) for any given mouse after segments containing artifacts were rejected.

Statistical analysis and definition of movement states

All statistical analysis was performed as described previously (Lovelace *et al.* 2018; Lovelace *et al.* 2019). Statistical group comparisons of chirp responses (ITPC and STP) were quantified by wavelet analysis using MATLAB (MATLAB, RRID:SCR_001622). The analysis was conducted by binning time (2 s segments) into 256 parts and frequency into 100 parts, resulting in a 100 x 256 matrix. Non-parametric cluster analysis was used to determine contiguous regions in the matrix that were significantly different from a distribution of 2000 randomized Monte Carlo permutations based on previously published methods (Maris & Oostenveld 2007). Briefly, if the cluster size of the real genotype assignments (both positive and negative direction, resulting in a two-tailed alpha of p=0.025) were larger than 97.25% of the

random group assignments, those clusters were considered significantly different between genotypes. This method avoids statistical assumptions about the data and corrects for multiple comparisons. In all cases, $p<0.05$ was considered significant for ANOVA and Student's t-tests. Where t-tests were performed, r was calculated as an effect size. When interactions were found and multiple comparisons for ANOVA were made, data were analyzed on each factor for simple effects and corrected using Bonferroni adjustments. If assumptions of sphericity were violated for repeated measures ANOVA, the Greenhouse-Geiser correction was used.

As movement can alter cortical gain (Niell & Stryker 2010), and *Fmr1* KO mice show hyperactivity, a piezoelectric transducer was placed under the EEG recording arena to detect when the mouse was moving. The term 'resting' is used to indicate EEGs recorded in these mice without any specific auditory stimuli. The term 'still' is used to describe resting EEG when the mouse was stationary. The term 'moving' is used to describe resting EEG when the mouse was moving based on a threshold criterion for the piezoelectric signal that was confirmed by analyzing the video recording (under IR light) that was taken throughout the EEG recording procedure. In all cases where genotype means are reported, SEM was used. The genotype differences in resting power were analyzed on 6 dependent variables using one-way Multivariate analysis of co-variance (MANCOVA) with one covariate (movement), Independent Variables (IV): Genotype (*Fmr1* KO, WT), dependent variables (DV): 6 frequency bins (delta to high gamma). The proportion of time spent moving during the five-minute recording session was used as a covariate to isolate effects of genotype and control for the effect movement has on cortical gain. When multiple comparisons for MANCOVA were made, genotype comparisons were corrected using Bonferroni adjustments. The divisor for Bonferroni correction for multiple comparisons (for 6 frequency bands) on MANCOVA was set to 6, $\alpha = 0.05/6 = 0.0083$. Data are

often expressed and plotted as ratio of control group values to gauge relative differences in various factors using the same scale. Statistical analysis was done using SPSS software package (SPSS, RRID:SCR_002865).

Treatment

The matrix metalloproteinase 2/9 inhibitor, SB-3CT, in saline containing 10% DMSO (Millipore, Cat. 444274), or vehicle (10% DMSO in saline) was administered intraperitoneally (i.p., 25 mg/kg) to WT and *Fmr1* KO mice at P22-23 (for timeline see Figure 1A). For treatment, animals were assigned treatment based on simple randomization. To blind experimenter to treatment, animals were given a numerical identifier with no treatment identification that was used during EEG recording and PV/PNN analysis. A second group of mice that did not undergo EEG surgery or recording received a single treatment of SB-3CT (25 mg/kg) or vehicle injections at P27-28 and were subjected to behavioral tests at P28-29 (Figure 6A). To blind experimenter to treatments during behavior, tests were performed by two experimenters, one experimenter administered treatment and second experimenter was blinded to assigned treatment of each mouse. A third group that did not undergo EEG surgery or recording received a single treatment of SB-3CT (25 mg/kg) or vehicle injections at P21-22 (Figure 7A). To blind experimenter to treatments, one experimenter prepared drugs and assigned a numerical identifier to each treatment/animal and a second experimenter administered the treatment and was blinded to each assigned treatment. Initial number of animals used per group: EEG implant surgery (WT, N=35; *Fmr1* KO, N=30), EEG recording (WT PRE, N=23; *Fmr1* KO PRE, N=21; vehicle-treated WT, N=18; SB-3CT-treated WT, N=15; vehicle-treated *Fmr1* KO, N=14; SB-3CT-treated *Fmr1* KO, N=13;), PV/PNN analysis (N=6 per group; vehicle-treated WT, n=18; SB-3CT-treated WT, n=23; vehicle-treated *Fmr1* KO, n=20; SB-3CT-treated *Fmr1* KO, n=17),

behavior (vehicle-treated *Fmr1* KO, N=10; SB-3CT-treated *Fmr1* KO, N=9; vehicle-treated WT, N=10; SB-3CT-treated WT, N=8), Western blot (vehicle-treated *Fmr1* KO, N=4; SB-3CT-treated *Fmr1* KO, N=4; vehicle-treated WT, N=4; SB-3CT-treated WT, N=4), DQ gelatin assay (vehicle-treated *Fmr1* KO, N=5; SB-3CT-treated *Fmr1* KO, N=5; vehicle-treated WT, N=3; SB-3CT-treated WT, N=3).

Dye-Quenched (DQ) Gelatin Assay and Analysis

The dye-quenched (DQ) gelatinase activity assay is a hydrolytic activity assay used to measure MMP-2/9 activity. The DQ gelatin assay measures MMP-2/9 activity by measuring the fluorescent intensity of a FITC-quenched gelatin peptide that fluoresces following cleavage by MMP-2 or MMP-9 to measure MMP-2/MMP-9 proteolytic activity (Vandooren *et al.* 2011). To confirm that i.p. administration of SB-3CT results in the inhibition of MMP-9 activity in the brain, one hour after treatment with SB-3CT inhibitor or vehicle P22 WT mice (N=3 per group) were euthanized with isoflurane and the auditory cortex and surrounding temporal cortex (average weight of tissue ~20 mg) was dissected based on coordinates (Paxinos and Franklin 2004) and previous electrophysiological and dye-placement studies (Martin del Campo *et al.* 2012). For an example of auditory cortex dissection, please see Supplemental Figure 2-1. The one-hour time point was chosen based on the ~45 min half-life of SB-3CT (Gooyit *et al.* 2012). The AC was resuspended in lysis buffer (50mM Tris-HCL (pH = 7.4) buffer containing 150mM NaCl, 5mM EDTA,, 0.05% Triton X-100, 1mM PMSF) containing protease inhibitor cocktail (Sigma-Aldrich, cat. #P8340) and phosphatase inhibitor cocktail (Sigma-Aldrich, cat. #P0044). Lysates were measured for total protein concentrations using the protocol for the BCA colorimetric protein assay (Pierce, cat. #23-235).

Lysates were diluted in reaction buffer and mixed with DQ-gelatin stock, a fluorescence-labeled gelatin substrate (Molecular Probes, E12055) as described previously (Lovelace *et al.* 2019). Lysates were coded and processed by experimenter blinded to codes. Fluorescence intensity was analyzed using 495nm excitation wavelength and 515nm emission wavelength in a fluorescence microplate reader equipped with standard fluorescein filters (SpectraMax M2, Molecular Devices). The signal from the samples was measured every 20 min during a 3h incubation period. For each time point, background fluorescence intensity was corrected by subtracting the values derived from the blank, which consisted of only reaction buffer and DQ gelatin. A standard curve to assess gelatinase activity was generated using recombinant mouse MMP-9 activity (rmMMP-9, specific activity approx. 1,500 pmol/min/µg, R&D Systems, Cat. # 909-MM-010)**.** A linear regression of rmMMP-9 activity (standard curve) and relative gelatinase activity based on the average fluorescence intensity of three replicates was used to assess gelatinase proteolytic activity in the lysates.

Immunohistochemistry

For histology, mice were euthanized with isoflurane and perfused transcardially with ice-cold phosphate-buffered saline (0.1 M PBS, pH 7.4) and 4% paraformaldehyde (PFA). Brains were sectioned in the coronal plane on a Vibratome (Leica S1000) at 100 µm and sections were stored in PBS before staining. Prior to immunostaining, free-floating sections were post-fixed for an additional 2 h in 4% PFA and then washed in 0.1M PBS. Sections were then quenched with 50mM ammonium chloride for 15 min, permeabilized with 0.1% Triton X-100 for 10 min and blocked for 1 h at room temperature in 5% donkey serum (DS; Sigma-Aldrich Cat# D9663, RRID:AB_2810235), and 1% bovine serum albumin (BSA; Fisher Scientific, Catalog #9048468) in 0.1M PBS. Sections were incubated overnight in primary antibodies and a 1:500 dilution of

fluorescein-tagged *Wisteria floribunda* Lectin (4µg/mL WFA, Vector Laboratories Cat# FL-1351, RRID: AB_2336875) in a 1% DS, 0.5% BSA, and 0.1% Tween-20 solution. Primary antibodies included a 1:1000 dilution of mouse anti-PV antibody (Sigma-Aldrich Cat#P3088, RRID:AB_477329) to label PV interneurons. Sections were incubated in a 1:500 dilution of donkey anti-mouse Alexa Fluor 594 for 1 h. After immunostaining sections were mounted on slides and cover slipped with Vectashield containing DAPI (Vector Laboratories Cat#H-1200, RRID:AB_2336790) and Cytoseal (ThermoScientific, Catalog #8310-16).

Image Quantification

Slices were imaged by confocal microscopy (model LSM 510, Carl Zeiss MicroImagining or Leica SP5) using a series of 10 high-resolution optical sections (1024 x 1024-pixel format) that were captured for each slice at 10X magnification at 1µm step intervals (z-stack). All images were acquired under identical conditions. Each z-stack was collapsed into a single image by projection (ImageJ), converted to a TIFF file and encoded for blind analysis using ImageJ (NIH software, ImageJ, RRID:SCR_003070). The AC was identified using hippocampal landmarks (Supplemental Figure 2-1). This method has been previously validated using tonotopic mapping and dye injection (Martin del Campo *et al.* 2012) and comparison with the Paxinos mouse atlas and other publications on the mouse AC (Anderson *et al.* 2009). Nevertheless, the precise boundary between primary AC (A1) and anterior auditory field (AAF) of the mouse AC cannot be clearly established. Both these fields are part of the lemniscal auditory system and comprise the core AC. Therefore, we use the AC to indicate both A1 and AAF. ImageJ was used to identify and count PNN-positive, PV-positive cells and PV/PNN co-localization (N=6 per group; vehicle-treated WT, n=18; SB-3CT-treated WT, n=23; vehicle-treated *Fmr1* KO, n=20; SB-3CT-treated *Fmr1* KO, n=17) . Cortical layers were identified

(Anderson *et al.* 2009) and used for layer-specific counts (Layers 1-5/6 of the AC). A selection tool was used to measure and specify layers of the AC and the point tool was used to label PNNs, PV cells and added to the ROI manager.

Behavior

Open-field test

Behavioral tests were performed as described previously (Sidhu *et al.* 2014; Lovelace *et al.* 2019). Briefly, anxiety-like behavior was tested in P27-28 mice (N=6-7 per group) by quantifying their tendency to travel to the center of an open field and time spent in thigmotaxis (Yan *et al.* 2005; Yan *et al.* 2004). A 43cm x 43cm open-field arena with 43-cm-high walls was constructed from clear acrylic sheets. The open field arena was placed in a brightly lit room, and one mouse at a time was placed in a corner of the open field and allowed to explore for 10 min while being recorded with digital video from above. The floor was cleaned with 3% acetic acid, 70% ethanol and water between tests to eliminate odor trails. The mice were tested between the hours of 8:00 AM and 1:00 PM., and this test was always performed prior to the elevated plus maze by the same experimenter. The arena was subdivided into a 4 x 4 grid of squares with the middle of the grid defined as the center. A line 4 cm from each wall was added to measure thigmotaxis. Locomotor activity was scored by the analysis of total line crosses and speed as described previously with some modifications (Yan *et al.* 2005) using TopScan Lite Software (Clever Sys., Inc., Reston, VA 201090, USA). A tendency to travel to the center (total number of entries into large and small center squares) and the time in thigmotaxis were used as an indicator of anxiety-like behaviors using TopScan Lite software (CleverSys Inc). The analysis was performed in 5 min intervals for the total 10 min exploration duration. Assessments of the digital recordings were performed blind to the condition. Statistical analysis was performed with

unpaired t-test using GraphPad Prism 6 software. Data represent mean ± standard error of the mean (SEM).

Elevated plus maze

The elevated plus maze consisted of four arms in a plus configuration. Two opposing arms had 15-cm tall walls (closed arms), and two arms were without walls (open arms). The entire maze sat on a stand 1 m above the floor. Each arm measured 30 cm long and 10 cm wide. Mice were allowed to explore the maze for 10 min while being recorded by digital video from above. The maze was wiped with 3% acetic acid, 70% ethanol and water between each test to eliminate odor trails. This test was always done following the open-field test. TopScan Lite software was used to measure the percent of time spent in open arms and speed. The time spent in open arm was used to evaluate anxiety-like behavior. The velocity and total arm entries were measured to evaluate overall locomotor activity. The analysis was performed in 5 min intervals for the total 10 min exploration duration. Assessments of the digital recordings were done blind to the condition using TopScan Lite software. Statistical analysis was performed with unpaired t-test using GraphPad Prism 6 software. Data represent mean ± standard error of the mean (SEM).

Western Blot Analysis

Western blot analysis was performed as described previously (Lovelace *et al.* 2019). The AC was removed from each mouse (N=3-4 mice per group), cooled in PBS, and homogenized in ice-cold lysis buffer (50mM Tris-HCl, pH 7.4, 150mM NaCl, 5mM EDTA, 0.05% Triton X-100, and 1mM PMSF) containing protease inhibitor cocktail (Sigma-Aldrich, cat. # P8340) and phosphatase inhibitor cocktail (Sigma-Aldrich, cat. #P0044). The samples were rotated at 4°C for at least 1h to allow for complete cell lysis and then cleared by centrifugation at 13,200 rpm for 15min at 4°C. Supernatants were isolated and boiled in reducing sample buffer (Sigma-

Aldrich, Laemmli 2× concentrate, S3401), and separated on 8–16% Tris-Glycine SDS-PAGE precast gels (EC6045BOX, Life Technologies). Proteins were transferred onto Protran BA 85 Nitrocellulose membrane (GE Healthcare) and blocked for 1h at room temperature in 5% skim milk (catalog #170-6404, Bio-Rad). Primary antibody incubations were performed overnight at 4°C with antibodies diluted in TBS/0.1% Tween-20/5% BSA. The following primary antibodies were used: rabbit anti-Akt (Cell Signaling Technology Cat# 9272, RRID:AB_329827); rabbit anti-phospho-Akt (Ser473; Cell Signaling Technology Cat# 9271, RRID: AB_329825); mouse anti-PV (Millipore, Cat#MAB1572, RRID:AB_2174013), mouse anti-total TrkB (1:2000; BD Biosciences Cat# 610101, RRID:AB_397507), rabbit anti-phospho-TrkB (Tyr515) (1:1000, Bioworld, catalog #AP0236), and rabbit anti-βactin at 1:2000 (Abcam Cat #ab8227, RRID:AB_2305186). All primary antibodies were from Cell Signaling Technology and used at a dilution of 1:1000, unless stated otherwise.

Blots were washed 3 × 10 min with TBS/0.1% Tween-20 and incubated with the appropriate HRP-conjugated secondary antibodies for 1h at room temperature in a TBS/0.1% Tween-20/5% BSA solution. The secondary antibodies used were HRP-conjugated donkey anti-mouse IgG (Jackson ImmunoResearch Labs Cat#715-035-150, RRID:AB_2340770) or HRP-conjugated goat anti-rabbit IgG (Jackson ImmunoResearch Labs Cat# 111-035-003, RRID:AB_2313567). After secondary antibody incubations, blots were washed 3 × 10min in TBS/0.1% Tween-20, incubated in ECL 2 Western Blotting Substrate (Thermo Scientific, catalog #80196) and a signal was collected with CL-XPosure film (Thermo Scientific, catalog #34090). For re-probing, membrane blots were washed in stripping buffer (2% SDS, 100mM β-mercaptoethanol, 50mM Tris-HCl, pH 6.8) for 30min at 55°C, then rinsed repeatedly with TBS/0.1% Tween-20, finally blocked with 5% skim milk, and then re-probed. Developed films

were then scanned, and band density was analyzed by measuring band and background intensity using Adobe Photoshop CS5.1 software (Adobe Photoshop, RRID:SCR_014199). Four-five samples per group of vehicle vs. SB-3CT WT vs. *Fmr1* KO were run per blot. Statistical analysis was performed with unpaired t-test using GraphPad Prism 6 software (GraphPad Prism, RRID:SCR_002798). Data represent mean ± standard error of the mean (SEM).

Statistical Analysis

All statistical analyses for cell density quantification, Western blot, behavior and DQ gelatin assay were done using Prism (GraphPad Software, San Diego, USA). For cell density quantification, theta/gamma ratio, and behavior two-way ANOVA was used to compare Genotype (WT x KO) vs. Treatment (SB-3CT x Vehicle) followed by *post hoc* pair-wise comparisons with the Bonferroni's or Tukey's correction, unless otherwise specified. For Western blot and the DQ gelatin assay, the Student's t-test was used to assess the effects of treatment in KO or WT mice. For all analyses, "N" = number of animals and "n" = number of coronal sections. No power analysis was performed to calculate sample size for each experiment. The number of animals for each study was determined using previously published studies using similar techniques [EEG (Lovelace *et al.* 2018; Wen *et al.* 2019), PV/PNN analysis (Lovelace *et al.* 2019; Wen *et al.* 2018), behavior and DQ gelatin (Lovelace *et al.* 2019)].

Results

In the current study, we examined whether acute pharmacological inhibition of MMP-9 activity during a developmental critical period reduces correlates of auditory hypersensitivity in developing *Fmr1* KO mice. First, we evaluated changes in spectral power and synchronization to auditory stimuli using EEG, as well as changes in PV/PNN density. Next, we assessed anxiety-

like behaviors and hyperactivity along with changes in key molecular targets associated with FXS, including PV levels and phosphorylation of TrkB and Akt.

Developing *Fmr1* KO mice exhibit increased resting state gamma EEG power and abnormal EEG power coupling

Previously, we have shown that adult *Fmr1* KO mice exhibit increased resting state gamma power (Lovelace *et al.* 2018), a phenotype that is similar to that observed in humans with FXS (Ethridge *et al.* 2017; Wang *et al.* 2017). Here, we assessed whether developing *Fmr1* KO mice on C57BL/6 background [for FVB background, see (Wen *et al.* 2019)], also exhibit increased resting state gamma power during the P21-28 period when maturation of various neuronal circuits occurs. To do this, mice were implanted with 2-channel EEG electrodes placed in the auditory (AC) and frontal cortex (FC) at P18 (Figure 1A and 1B), allowed to recover for 4-5 days, and baseline EEG activity was recorded at P22 prior to treatment (PRE). Resting EEG data (in the absence of auditory stimulation) were collected for five minutes and were divided into 2-second segments for spectral analysis. Resting EEG raw power ($\mu V^2/Hz$) was calculated in the AC and FC of WT and *Fmr1* KO mice by analyzing all frequency bands during the entire five-minute resting period. Examples of one-second segments of EEG traces for individual WT and *Fmr1* KO mice are shown in Figure 1C and 1D, respectively (AC: top; FC: bottom). The group average power spectral densities for the AC and the FC are shown in histogram (Figure 1E) and bar graph format (Figure 1F), respectively. To normalize data for each region and to determine relative changes in power across frequency bands, power values were expressed as a ratio of *Fmr1* KO (N=20) to WT (N=22) means (for non-normalized data see Supplemental Figure 1-1). A value of 1 indicates no mean difference in power between WT and *Fmr1* KO, while values above 1 indicate *Fmr1* KO > WT, and below indicate *Fmr1* KO < WT mice.

Statistical analysis was performed using a one-way MANCOVA with the percentage of time spent moving as a covariate. We compared genotype mean differences on six bands per region: Delta (1-4 Hz), Theta (4-8 Hz), Alpha (8-13 Hz), Beta (13-30 Hz), Low Gamma (30-55 Hz), and High Gamma (65-100 Hz). Frequencies from 55-65 Hz were excluded in all analysis, as a 60 Hz notch filter was utilized to eliminate line noise. We confirmed assumptions of equality of covariance using Levene's test of equality of error variance and no differences between genotypes were observed in error variance (all $p>0.05$). Since assumptions were not violated, we report an effect of genotype (AC: Pillai's Trace =2.465, $p=0.04$; FC: Pillai's Trace = 2.587, $p=0.036$) across all six of the combined frequency variables. The low gamma band was the only frequency band significantly different between genotypes in the AC and FC (Figure 1F; AC: low gamma, $F(1,27)=10$, $p=0.003$, $\eta^2=0.204$, FC: low gamma, $F(1,27)=9.012$, $p=0.005$, $\eta^2=0.188$; WT N=22, *Fmr1* KO N=20; for all frequency averages see Supplemental Table 1). These results indicate that *Fmr1* KO mice exhibit increased resting state low gamma power (30-55 Hz) early in development at P22-23.

Human EEG studies also report power abnormalities in delta, theta, alpha frequencies and impaired coupling between low and high frequency oscillations in individuals with FXS and ASD (Wang *et al.* 2013; Sinclair *et al.* 2017). To determine if there are abnormalities in power coupling in early development, a Pearson's correlation was done during the resting baseline period to assess the relationship between power across different frequencies and/or regions, using the same approach that was used in a study for human FXS (Wang *et al.* 2013). Results show a negative correlation in power coupling of the AC Theta/Low Gamma and AC Alpha/Low Gamma in WT mice (Figure 1G). These correlations were significantly reduced in *Fmr1* KO mice (T1G1: $p=0.02$; A1G1: $p=0.008$). Results also show a negative correlation in across region

power coupling of the AC Theta/FC Low Gamma and AC Alpha/FC Low Gamma in WT mice (Figure 1I), and FC Theta/AC Low Gamma and FC Alpha/AC Low Gamma (Figure 1J). These correlations were also significantly reduced in *Fmr1* KO mice (T1G2: p=0.03; A1G2: p= 0.04; T2G1: p=0.04; A2G1: p=0.03).

Overall, these findings indicate that abnormalities in resting gamma power and EEG power coupling, in particular changes in theta/low gamma and alpha/low gamma power coupling in the AC and cross regional impairments are present in developing *Fmr1* KO mice as early as P22-23.

Fmr1 KO mice treated with MMP-9 inhibitor show no effect on resting state EEG gamma power and EEG power coupling

Next, both *Fmr1* KO and WT mice received a single i.p. injection of the MMP-2/9 inhibitor, SB-3CT (25mg/kg), or vehicle immediately following EEG recording to assess the efficacy of acute MMP-9 inhibition to normalize resting EEG oscillation pattern (Figure 1A). One day after treatment, resting EEG baseline data was again collected for 5 min and was divided into 2-second segments for spectral analysis. The percentage of time that the mice spent moving during the recording period was not different between genotypes (Supplemental Figure 1-2) or treatment groups (Supplemental Figure 2-7). Figure 2 shows the average spectral power as a ratio of the corresponding control group in histogram (Figure 2A-C) and bar graph format (Figure 2D-F) for each group (AC: top; FC: bottom; for non-normalized data see Supplemental Figure 2-2). To determine resting EEG in vehicle groups, vehicle-treated *Fmr1* KO mice were compared to vehicle-treated WT mice. Although resting state low (LG) and high gamma (HG) power was trending higher in the AC of vehicle-treated *Fmr1* KO (N=12) compared to vehicle-treated WT (N=16) mice, this was not statistically significant possibly due to large variability in

vehicle-injected *Fmr1* KO mice (Figure 2D; also see Supplemental Figure 2-4). Although SB-3CT-treated *Fmr1* KO (N=12) mice exhibited normal low and high gamma in the AC and FC that was comparable to SB-3CT-treated WT (N=15) mice (Figure 2E), comparison of SB-3CT-treated *Fmr1* KO (N=12) mice to vehicle-treated *Fmr1* KO (N=12) mice showed a trending reduction in low and high gamma power, but this was not statistically significant (Figure 2F; for summary of all frequency averages see Supplemental Table 2). Vehicle-treated WT mice (N=16) and SB-3CT-treated WT mice (N=15; for non-normalized data see Supplemental Figure 2-3) did not show any significant changes in spectral frequencies compared to WT mice before treatment (PRE) in AC or FC [Supplemental Figure 2-5A and 2-5D (Vehicle-WT) and Supplemental Figure 2-5B and 2-5E (SB-3CT-WT)].

To determine if EEG power coupling abnormalities were ameliorated following treatment with SB-3CT, a Pearson's correlation was done during the resting baseline period to assess the relationship between power across different frequencies and/or regions. Results show that treatment with SB-3CT did not alter the EEG power coupling profiles in WT or *Fmr1* KO mice (Supplemental Figure 2-6).

Together, these results indicate no significant effects of treatment in *Fmr1* KO mice when resting EEG power or EEG power coupling was analyzed for individual frequencies between vehicle- and SB3CT-treated groups.

Phase Locking to Auditory "Up Chirp" stimuli is impaired in developing *Fmr1* KO mice

To assess whether P22-23 *Fmr1* KO mice also exhibit deficits in the consistency of phase locking to time varying stimuli as seen in adult *Fmr1* KO mice (Lovelace *et al.* 2018), and humans with FXS (Ethridge *et al.* 2017), we recorded responses to chirp stimuli. We tested both up and down chirps to ensure that the differences are specific to modulation frequencies and are

not affected by the direction of frequency change in the sound (Lovelace *et al.* 2019). Following EEG resting state baseline recording, repeated chirp stimuli (300 trials for up, 300 trials for down) was delivered and electrocortical activity was recorded. Inter trial phase coherence (ITPC) was calculated across trials in the time x frequency domain using Morlet Wavelet analysis (Lovelace *et al.* 2018). After grand average ITPC was calculated for each group, we found EEG oscillations that matched the frequency of the chirp and were seen as increased ITPC along a diagonal, from 0 to 2 s and 1-100Hz. The means for WT PRE (Figure 3A; only 'up chirp' data are shown) were subtracted from *Fmr1* KO PRE mice (Figure 3B) to show the difference between *Fmr1* KO and WT (Figure 3C) in the AC (top) and FC (bottom). For statistical analysis, clusters of p-values were calculated, and significant differences ($p<0.025$) were overlaid on the chirp response to demonstrate quantitative differences between each genotype after correction for multiple comparisons (Lovelace *et al.* 2019). We observed a statistical difference between genotypes in one main cluster, which spans the low gamma band ITPC in both the AC (35-55 Hz) and FC (35-65 Hz; significant clusters are highlighted by bold-lined contours in Figure 3C. In the FC, there was also a statistical difference between genotypes in the high gamma band in the FC (80-100 Hz). Similar patterns of statistics of ITPC were observed for both up and down chirps (down chirp data not shown).

To examine whether P22-23 *Fmr1* KO mice also exhibit an increase in background gamma power in both the AC and FC during the chirp presentation, similar to adult *Fmr1* KO mice (Lovelace *et al.* 2018), we assessed non-phase locked single trial power (STP) during chirp stimulation in *Fmr1* KO mice compared to WT control mice. Using the same statistical cluster analysis as for the chirp ITPC, results indicate that P22-23 *Fmr1* KO mice exhibit a significant

increase in background gamma power in the AC (~30-55 Hz) and FC (~30-70 Hz) compared to WT control mice (Figure 3D).

Together, these data show that developing *Fmr1* KO mice exhibit low and high gamma synchronization deficits and increased background gamma power in both the AC and FC in a manner similar to adult *Fmr1* KO mice and humans with FXS.

Acute MMP-9 inhibition improves phase-locking to time varying auditory stimuli in *Fmr1* KO mice

To test whether acute treatment of SB-3CT would ameliorate the ITPC deficit to the auditory chirp stimuli, both up and down chirps were presented during EEG recording one day after treatment. Figure 4A and 4B show grand average ITPC values for vehicle-treated and SB-3CT-treated *Fmr1* KO, respectively. The mean for vehicle-treated *Fmr1* KO mice was subtracted from vehicle-treated WT mice (Figure 4C) to show the difference between ITPC values in *Fmr1* KO and WT mice in both the AC and FC. Similarly, the mean for SB-3CT-treated *Fmr1* KO mice was subtracted from the mean of vehicle-treated *Fmr1* KO mice (Figure 4D). For statistical analysis, clusters of p-values were calculated, and these differences were overlaid on the chirp response to demonstrate quantitative differences between each genotype after correction for multiple comparisons. Monte Carlo statistical method on cluster analysis revealed a significant reduction in average ITPC values between vehicle-treated *Fmr1* KO (N=12) mice and vehicle-treated WT (N=17) mice in low gamma band range (~40-50 Hz) in the AC (Figure 4C: top), consistent with the reduction observed in un-treated mice (Figure 3D). Statistical analysis of average ITPC values shows a significant enhancement in the same low gamma band range (~40-50 Hz) ITPC in the AC of SB-3CT-treated *Fmr1* KO mice (N=12) to vehicle-treated *Fmr1* KO (N=12) mice (Figure 4D: top). However, a significant decrease in ~30-40 Hz gamma band range

ITPC band in both AC and FC was observed (time x frequency bands that are significantly different between groups are highlighted in bolded black lines). Grand average ITPC values were also calculated for vehicle-treated (N=17) and SB-3CT-treated WT (N=14) mice (Supplemental Figure 4-1A and 4-1B, respectively). No significant differences were detected in AC or FC for average ITPC values between vehicle-treated WT (N=17) mice and WT PRE (N=23) mice in the low and high gamma ITPC band except for a small decrease in the FC at ~25-35 Hz (Supplemental Figure 4-1C), suggesting the effects of injection on the ~25-35 Hz gamma band range. SB-3CT-treated WT (N=14) mice exhibited a significant increase in high gamma band ITPC in the AC, but not FC, specifically in 70-85 Hz ITPC band compared to WT PRE (Supplemental Figure 4-1D). Similar patterns and statistics of ITPC were observed for both up and down chirps. These results indicate that an acute treatment of the MMP-9 inhibitor, SB-3CT, improves fidelity of temporal responses to auditory stimuli by specifically increasing low gamma band (40-50 Hz) ITPC in developing *Fmr1* KO mouse cortex.

Acute inhibition of MMP-9 enhances PNN formation in the developing auditory cortex of *Fmr1* KO mice

Previously, we showed evidence for delayed development of PV interneurons and PNN formation around PV interneurons in layers 2-4 of the developing AC of *Fmr1* KO mice (Wen *et al.* 2018). Here we examined whether acute pharmacological inhibition of MMP-9 would ameliorate the PV/PNN deficits in P22-23 *Fmr1* KO mice. To test this, immediately after EEG recordings (one day after treatment), mice were sacrificed, and brains were collected for PV immunostaining and PNN labeling using *Wisteria floribunda* Agglutinin (WFA; Figure 1A, PV/PNN analysis). We analyzed the density of PV-positive (Figure 5A, 5E, 5I, 5M), PNN-positive (Figure 5B, 5F, 5J, 5N), and PV/PNN co-labeled neurons (Figure 5C, 5G, 5K, 5O) in

layer 4 of the AC contralateral to the EEG electrode (for layers 1, 2/3 and 5/6 see Supplemental Figure 5-1). We observed a significant increase of PNN density in SB-3CT-treated *Fmr1* KO mice compared to vehicle-treated *Fmr1* KO mice (Figure 5R, p=0.02). There was also a significant increase of PNN density in SB-3CT-treated WT mice compared to vehicle-treated WT mice (Figure 5R, p=0.009). Statistical analysis of PV/PNN co-localization revealed a significant increase of PV/PNN co-localization in SB-3CT-treated *Fmr1* KO mice compared to vehicle-treated *Fmr1* KO mice (Figure 5S, p=0.008). There was also a significant increase of PV/PNN co-localization in SB-3CT-treated WT mice compared to vehicle-treated WT mice (Figure 5S, p=0.04; for all average values and statistics see Supplemental Table 3-4).

Taken together, these data suggest that acute pharmacological inhibition of MMP-9 normalizes PNN development and co-localization of PNN predominantly around PV interneurons in layer 4 of the developing AC of *Fmr1* KO mice, consistent with improved phase locking at low gamma band frequencies.

Acute inhibition of MMP-9 ameliorates anxiety and hyperactivity in *Fmr1* KO mice

Next, we assessed whether SB-3CT treatment reduces anxiety-like behaviors and hyperactivity in *Fmr1* KO mice that received an i.p. injections of SB-3CT (25mg/kg) at P27-28 (for timeline see Figure 6A). Anxiety-like behaviors were assessed on P28-29 mice (one day after treatment) using the elevated plus maze (EPM) and open field (OF). In the EPM, mice were allowed to explore the cross-shaped field for 10 min. TopScan Live software was used to evaluate anxiety-like behaviors by determining the percent of time spent in the open arms (Figure 6B). To evaluate locomotor activity and hyperactivity, the number of total entries into open and closed arms (Figure 6C), and the average speed (Figure 6D) were quantified. Results showed that vehicle-treated *Fmr1* KO mice spent less time in the open arms compared to

vehicle-treated WT controls (Figure 6B). Statistical analysis using two-way ANOVA revealed significant effect of treatment, genotype, and significant interaction (for statistical comparisons refer to Supplemental Table 5). Post hoc comparisons showed that SB-3CT-treated *Fmr1* KO mice spent more time in open arms than vehicle-treated *Fmr1* KO mice (Figure 6B, $p<0.0001$). Treatment with SB-3CT did not alter behavior of WT mice, suggesting specificity of the drug to the *Fmr1* KO group. Vehicle-treated *Fmr1* KO mice also showed an increase in the number of total entries (Figure 6C, $p=0.0001$) and speed (Figure 6D, $p=0.0030$) compared to vehicle-treated WT controls. Treatment of *Fmr1* KO mice with SB-3CT reduced the number of total entries (Figure 6C, $p=0.0001$) and speed (Figure 6D, $p=0.0008$), yet it did not significantly alter the number of total entries or speed in WT controls (Figures 6C, 6D).

In the OF task, animals were allowed to explore an open field for 10 min. Anxiety-like behaviors were evaluated by measuring the total number of center entries (Figure 6E), the percent of time spent in thigmotaxis (Figure 6F), and the time spent in the center per entry (Figure 6G). Locomotor activity was assessed by determining the number of total line crosses (Figure 6H) and average speed (Figure 6I). All behaviors were quantified using TopScan Live software. Statistical analysis using two-way ANOVA revealed significant main effects of treatment and interaction (for statistical comparisons refer to Supplemental Table 5 and 6). Post hoc comparisons showed that vehicle-treated *Fmr1* KO mice made fewer center entries (Figure 6E, $p=0.0316$), spent more time in thigmotaxis (Figure 6F, $p<0.0001$) and spent less time in the center per entry (Figure 6G, $p=0.0173$) compared to vehicle-treated WT controls. However, SB-3CT-treated *Fmr1* KO mice made more center entries (Figure 6E, $p=0.0101$), spent less time in thigmotaxis (Figure 6F, $p<0.0001$) and more time in the center per entry (Figure 6G, $p=0.0086$) compared to vehicle-treated *Fmr1* KO mice. Statistical analysis using two-way ANOVA also

revealed a significant increase in the total line crosses (Figure 6H, $p<0.0001$) and average speed (Figure 6I, $p<0.0001$) in vehicle-treated *Fmr1* KO mice compared to vehicle-treated WT mice. SB-3CT treatment significantly decreased the total line crosses (Figure 6H, $p<0.0001$) and average speed (Figure 6I, $p=0.0021$; for all average values and statistics see Supplemental Table 5-6) of *Fmr1* KO mice. SB-3CT treatment did not change the behavior of WT mice in the open field.

These results suggest that acute inhibition of MMP-9 using SB-3CT alleviates anxiety/hyperactivity observed in *Fmr1* KO mice, without altering these behaviors in WT mice.

Acute inhibition of MMP-9 with SB-3CT reduces gelatinase activity and phosphorylation of Akt, while increasing PV levels and phosphorylation of TrkB

To confirm that the MMP-2/9 inhibitor, SB-3CT, reduced MMP-2/9 activity following treatment, gelatinase activity was measured using a Dye-Quenched (DQ) gelatin assay. *Fmr1* KO mice were injected with SB-3CT (25 mg/kg) or vehicle, the auditory and surrounding temporal cortex (Supplemental Figure 2-1) was collected and homogenized for the DQ gelatin assay 1 h post injection (for timeline see Figure 7A). A mouse recombinant MMP-9 (~1,500 pmol/min/µg) was used as a standard to calculate the approximate MMP-9 activity in the sample using a linear regression curve (Figure 7B). Results reveal that SB-3CT-treated *Fmr1* KO mice exhibit significantly decreased levels of gelatinase activity 1 h post injection compared to vehicle-treated *Fmr1* KO mice (Figure 7C, t-test, N=5 per group, $p=0.02$, Supplemental Table 7). SB-3CT-treated WT mice also show significantly reduced gelatinase activity compared to vehicle-treated WT mice (Supplemental Figure 7-1).

Previous studies have shown over-activation and enhanced phosphorylation of Akt/mTOR in the cortex of *Fmr1* KO mice (Lovelace *et al.* 2019), may underlie abnormalities in

synaptic functions and hyperexcitability (Klann & Dever 2004; Sharma *et al.* 2010). In addition, genetic deletion of MMP-9 restored Akt/mTOR phosphorylation to the normal levels in the hippocampus of *Fmr1* KO mice, while treatment of WT neurons with active MMP-9 enhanced Akt/mTOR phosphorylation (Sidhu *et al.* 2014). Therefore, to determine whether acute pharmacological MMP-9 inhibition influenced Akt/mTOR-related signaling, we analyzed Akt phosphorylation in the AC of SB-3CT and vehicle-treated *Fmr1* KO mice. *Fmr1* KO mouse brains were collected for Western blot analysis at P27-28 immediately after behavior, one-day following treatment (for timeline see Figure 6A). Results show reduced levels of Akt phosphorylation in SB-3CT-treated *Fmr1* KO mice compared to vehicle-treated *Fmr1* KO mice (Figure 7D; $N = 4$, $t(6) = 4.274$, $P = 0.0235$, t-test). There were no significant changes in Akt phosphorylation in SB-3CT-treated compared to vehicle-treated WT mice (Supplemental Figure 7-2A).

As TrkB signaling is implicated in PV cell development and survival (Nomura *et al.* 2017; Xenos *et al.* 2018), we examined the effects of acute MMP-9 inhibition on PV levels and phosphorylation of TrkB using Western blot. Results show that following SB-3CT treatment *Fmr1* KO mice exhibit increased PV levels (Figure 7E; $N = 4$, $t(6) = 2.607$, $P = 0.0479$, t-test). We also observed an increase in TrkB phosphorylation on Tyrosine (Y) 515 in SB-3CT treated *Fmr1* KO mice compared to vehicle-treated *Fmr1* KO mice (Figure 7F; $N = 4$, $t(6) = 2.805$, $P = 0.0378$, t-test), while there was no significant change in total TrkB levels (Figure 7G; for average values see Supplemental Table 8). Comparison of SB-3CT-treated WT versus vehicle-treated WT mice did not reveal any significant changes in PV (Supplemental Figure 7-2B), pTrkBY515 (Supplemental Figure 7-2C), or total TrkB (Supplemental Figure 7-2D).

Discussion

In this study, we show that P22-23 *Fmr1* KO mice exhibit abnormal neural oscillation patterns that parallel adult *Fmr1* KO mice and humans with FXS including increased resting state gamma power and deficits in gamma synchronization to auditory stimuli. Treatment with the MMP-9 inhibitor, SB-3CT, had no significant effect on resting EEG power or EEG power coupling in *Fmr1* KO mice. However, acute inhibition of MMP-9 activity improved fidelity of gamma frequency (~40 Hz) phase locking to time varying auditory stimuli in SB-3CT *Fmr1* KO mice compared to vehicle-treated *Fmr1* KO mice. At the molecular level, SB-3CT treatment enhanced PNN formation predominantly around PV interneurons in the developing AC of both *Fmr1* KO mice and WT mice. Assessment of anxiety/hyperactivity with EPM and OF tests demonstrated that acute inhibition of MMP-9 activity ameliorated anxiety-like behaviors and hyperactivity in *Fmr1* KO mice. Lastly, acute inhibition of MMP-9 activity reduced Akt phosphorylation, while increasing PV levels and TrkB phosphorylation. Our data are consistent with previously reported benefits of minocycline treatment in humans with FXS (Schneider *et al.* 2013), *Fmr1* KO mice (Bilousova *et al.* 2009; Dansie *et al.* 2013; Toledo *et al.* 2019), and the *Drosophila* FXS model (Siller & Broadie 2011), and further suggest that minocycline may alleviate FXS symptoms by suppressing MMP-9. These data support the notion that cellular and electrophysiological abnormalities of sensory processing are present early in development. In addition, treatment during early postnatal developmental period may be beneficial in ameliorating deficits due to higher cortical plasticity. Furthermore, reduction of MMP-9 activity may provide a suitable target to reduce auditory hypersensitivity in FXS and potentially other ASDs.

Developing and adult *Fmr1* KO mice exhibit comparable EEG phenotypes

In this study, we show that developing *Fmr1* KO mice (P22-23) exhibit increased resting state low gamma power in both the AC and FC (Figure 1) similar to adult *Fmr1* KO mice. Unlike adult *Fmr1* KO mice, though, developing *Fmr1* KO mice do not exhibit increased resting state delta or high gamma power (Lovelace *et al.* 2018). These results are consistent with data from the FVB strain of mice (Wen *et al.* 2019), suggesting that abnormal electrophysiological phenotypes are observed as early as P22 in developing *Fmr1* KO mice. The consistency of EEG phenotypes across age and genetic backgrounds of mice, and between humans and mice, indicate that these measures can be utilized as objective physiological biomarkers to test the effectiveness of potential drugs. Furthermore, accumulating evidence indicates that increased resting state gamma power is associated with sensory processing and communication deficits in FXS and ASD (Ethridge *et al.* 2017; Wang *et al.* 2017; Sinclair *et al.* 2017; Lovelace *et al.* 2018; Ethridge *et al.* 2019; Lovelace *et al.* 2019). Additional studies also point to abnormalities in theta and alpha power as contributing mechanisms underlying hyperexcitability (Van der Molen & Van der Molen 2013). Theta power is linked to cortical arousal level (Barry *et al.* 2009). Alpha power has been interpreted to reflect a neural inhibitory mechanism that regulates the processing of external, sensory information (Klimesch 1999; Mathewson *et al.* 2011). In particular, GABAergic inhibitory activity is thought to contribute to this neural inhibition mediated by alpha oscillations (Jensen & Mazaheri 2010). Together, alpha/theta synchronization have been linked to cognitive function (Klimesch 1999) and ability to inhibit irrelevant sensory information (Van der Molen & Van der Molen 2013). Human EEG studies report an inverted U-shaped pattern of power abnormalities showing reduced alpha frequencies, but increased delta, theta frequencies and high frequency bands (beta, gamma) in children with ASD (Wang *et al.* 2013; Sinclair *et al.* 2017). Elevated theta and delta power and reduced alpha power is also observed in

individuals with ADHD (Barry *et al.* 2003; Born *et al.* 2017). Our study shows a reduced EEG power correlations between Theta and Low Gamma, Alpha and Low Gamma bands within the AC as well as across regions (AC to FC and FC to AC) in *Fmr1* KO mice compared to WT mice. Overall, our findings indicate that abnormalities in EEG oscillation pattern, which are associated with hyperexcitability, cognitive performance, and ability to process sensory information, are present in developing *Fmr1* KO mice as early as P22-23.

In this study, we show that developing *Fmr1* KO mice exhibit decreased ability to produce synchronous stimulus-induced oscillations, similar to adult *Fmr1* KO mice (Lovelace *et al.* 2018), but the impairment is localized specifically to the low gamma frequencies (~30-55 Hz) in the AC and both low and high gamma (~65-100 Hz) frequencies in the FC. Treatment of *Fmr1* KO mice with SB-3CT leads to an improvement in phase locking to auditory chirp stimuli, in the same frequency range (~40-50 Hz) where the deficit was observed in vehicle-treated *Fmr1* KO AC (Figure 4). This result indicates that SB-3CT may be targeting specific cellular and network mechanisms in the AC resulting in improved phase locked synchronization in developing *Fmr1* KO mice.

Molecular mechanisms influencing *Fmr1* KO EEG phenotype

It is possible that changes in PV/PNN networks affect inhibitory circuits and neural oscillation patterns. The loss of PNNs is associated with abnormal plasticity and reduced excitability of PV interneurons (Balmer 2016; Lensjo *et al.* 2017; Chu *et al.* 2018). This may lead to altered balance of excitatory and inhibitory circuits, and improper network synchronization and hyperexcitability (Contractor *et al.* 2015). In fact, several studies point altered functionality of GABAergic circuits, specifically fast-spiking PV interneurons in FXS (Selby *et al.* 2007; Nomura *et al.* 2017; Goel *et al.* 2018). Specifically, PV cell density is

significantly reduced in the AC (Wen *et al.* 2018; Kulinich *et al.* 2019) and somatosensory cortex (Selby *et al.* 2007) of *Fmr1* KO mice compared to WT mice. One recent study demonstrated that passive developmental sound exposure during the maturation of synaptic and intrinsic properties (P9-21) results in enhanced PV cell density and PV/PNN co-localization in the AC of *Fmr1* KO mice despite impairment of PNN formation (Kulinich *et al.* 2019). In contrast, genetic reduction of MMP-9 was shown to enhance the formation of PNNs around PV cells in the AC (Wen *et al.* 2018). Our study shows that pharmacological inhibition of MMP-9 activity alone during the critical developmental period results in enhanced PNN formation around PV interneurons. While we did not see a significant increase in PV cell density, we did observe an increase in PV levels measured by Western blot, similar to what has been observed in other ASD models (Filice *et al.* 2016). It is possible that increased PNN formation around PV cells contributed to increased PV levels, which influenced the changes in resting state EEG oscillations in SB-3CT-treated *Fmr1* KO mice (Yamada *et al.* 2015). To more effectively target auditory hypersensitivity a combination of sensory stimulation (Woo & Leon 2013; Kulinich *et al.* 2019) with pharmacological inhibition of MMP-9 activity (Bilousova *et al.* 2009) may yield a synergistic effect.

Other studies have employed sound exposure or mGluR5 inhibitors during the late postnatal window (P20-30) to rescue AC plasticity deficits and found that they were only able to rescue sound exposure-induced cortical map plasticity (size of A1 and response latency) when *Fmr1* KO mice were exposed to sound between P9-20 in conjunction with daily MPEP injections (Kim *et al.* 2013). It is possible that inhibition of MMP-9 activity may function as a potent therapeutic for auditory hypersensitivity and anxiety/hyperactivity phenotypes during the critical developmental period. The question remains whether administration of SB-3CT during the

critical developmental period has more beneficial effects in regulating resting state EEG oscillations, improving responses to sound and anxiety/hyperactivity related behaviors in *Fmr1* KO mice *versus* administration of SB-3CT in adult *Fmr1* KO mice. SB-3CT has only ~45 min half-life (Gooyit *et al.* 2012). However, even transient inhibition of MMP-9 activity during this specific developmental window was sufficient to trigger structural and functional changes in the auditory cortex of *Fmr1* KO mice. One potential benefit may be attributed to the metabolism of SB-3CT, which functions as an irreversible inhibitor yielding covalent modifications that inhibit the activation of MMP-2/9 (Brown *et al.* 2000).

In addition to the enhanced PNN formation surrounding PV interneurons in the AC, the function of PV interneurons may also be influenced by activity of TrkB receptor. TrkB is shown to play a role in gamma-band synchronization in the hippocampal network (Zheng *et al.* 2011) and functions as a receptor for brain-derived neurotrophic factor (BDNF). In fact, TrkB is expressed by GABAergic neurons, in particular PV-positive cells (Lewis *et al.* 2005; Cellerino *et al.* 1996). BDNF-mediated signaling is involved in mediating cell growth and survival, neuronal differentiation, and activity-dependent regulation of inhibitory synapse development (Hong *et al.* 2008) and has been linked to maturation of PV cells in the cerebral cortex (Itami *et al.* 2007). BDNF via TrkB is known to promote the development of GABAergic neurons and induces the expression of GABA-related proteins, including GAD67, GAT1 and PV (Xenos *et al.* 2018; Nomura *et al.* 2017). Notably, BDNF-TrkB signaling has been shown to be impaired in *Fmr1* KO mice (Castren & Castren 2014). We previously reported decreased phosphorylation of TrkB in the AC of *Fmr1* KO mice compared to WT mice, which was up-regulated following developmental exposure to sound (Kulinich *et al.* 2019). In the current study, we showed that treatment with SB-3CT increased TrkB phosphorylation in *Fmr1* KO mice compared to vehicle-

treated *Fmr1* KO mice (Figure 7). Together, inhibition of MMP-9 activity may preferentially target PV-mediated inhibitory networks by influencing the stability of PV interneurons via increased PNN formation and activation of TrkB receptors.

Inhibition of MMP-9 activity reduces Akt phosphorylation and improves anxiety and hyperactivity phenotypes in *Fmr1* KO mice

FXS is characterized by over-activation of group I metabotropic glutamate receptors (Huber 2002), which promote Akt/mTOR signaling leading to aberrant phosphorylation of Akt and mTOR-related proteins, and increased protein synthesis (Sharma *et al.* 2010; Bear *et al.* 2004). Studies have shown that genetic reduction of p70 ribosomal S6 kinase 1 (S6K1) prevented elevated phosphorylation of translational control proteins, normalizing protein synthesis, reversing dendritic spine deficits, and improving social interactions, novel object recognition and behavioral flexibility in *Fmr1* KO mice (Bhattacharya *et al.* 2012). In fact, several studies link dysregulation of mTOR signaling with dendritic and synaptic abnormalities, cognitive impairments, and behavioral performance in FXS (Busquets-Garcia *et al.* 2014; Troca-Marin *et al.* 2012; Bhattacharya *et al.* 2012). Furthermore, treatment with the antibiotic minocycline, which is known to inhibit MMP-9, also promotes dendritic spine maturation and improves behavioral performance in developing *Fmr1* KO mice (Bilousova *et al.* 2009). Thus, it is possible that the reduction of Akt phosphorylation observed in *Fmr1* KO mice following treatment with SB-3CT may be linked to the changes in dendritic and synaptic profiles affecting protein synthesis, synaptic plasticity, and behavioral performance.

While *Fmr1* KO mice display multiple behavioral impairments that parallel human patients with FXS (Bernardet & Crusio 2006), there is wide variability in behavioral results assessing anxiety, hyperactivity, social and cognitive impairments in *Fmr1* KO mice. Several

studies find these measures to be altered (Sinclair *et al.* 2017; Bilousova *et al.* 2009; Ding *et al.* 2014), while others show no differences (Kazdoba *et al.* 2014). We show that vehicle-treated *Fmr1* KO mice spent less time in the open arms of the EPM, similar to previous studies in our lab (Bilousova *et al.* 2009), as well as increased percent time in thigmotaxis and decreased center entries in the OF, indicating higher anxiety. *Fmr1* KO mice also displayed increased hyperactivity indicated by increased speed in both EPM and OF tests. Interestingly, treatment with SB-3CT reduced both anxiety and hyperactivity measures in *Fmr1* KO mice. These results suggest that SB-3CT effectively ameliorates behavioral impairments observed in developing *Fmr1* KO mice when MMP-9 activity is inhibited during the specific developmental period.

In conclusion, we have shown that acute inhibition of MMP-9 activity during a specific critical developmental period (P22-P28) may serve to modulate PV neuron-mediated inhibitory circuits, neural oscillatory patterns, and behavioral impairments associated with FXS. These findings implicate MMP-9 as a potent candidate contributing to the FXS phenotype and indicate that targeted inhibition of MMP-9 activity may be a promising therapeutic agent.

Acknowledgements: Supported by National Institute of Mental Health, National Institute of Child Health and Human Development U54 HD082008-01. FRAXA Research Foundation Postdoctoral Fellowship to P.S.P and J.W.L and a University of California President's Postdoctoral Fellowship to P.S.P. Thank you to the Ethell, Binder, and Razak laboratories. A special thank you to all who contributed to the current research including Teresa H. Wen for training with surgeries, Carrie R. Jonak for assistance in mouse colony maintenance, Anna Kulinich for assistance in creating graphics and illustrations, and Dushan Rakic, Yasmien Hanania, Mark Makar, and Rashid Syed for technical assistance.

Conflict of Interest: The authors declare no competing financial interests.

References

Anderson, L. A., Christianson, G. B. and Linden, J. F. (2009) Mouse auditory cortex differs from visual and somatosensory cortices in the laminar distribution of cytochrome oxidase and acetylcholinesterase. *Brain Res* **1252,** 130-142.

Artieda, J., Valencia, M., Alegre, M., Olaziregi, O., Urrestarazu, E. and Iriarte, J. (2004) Potentials evoked by chirp-modulated tones: a new technique to evaluate oscillatory activity in the auditory pathway. *Clin Neurophysiol* **115,** 699-709.

Balakrishnan, S. and Pearce, R. A. (2014) Spatiotemporal characteristics and pharmacological modulation of multiple gamma oscillations in the CA1 region of the hippocampus. *Front Neural Circuits* **8,** 150.

Balmer, T. S. (2016) Perineuronal Nets Enhance the Excitability of Fast-Spiking Neurons. *eNeuro* **3**.

Barry, R. J., Clarke, A. R., Johnstone, S. J., McCarthy, R. and Selikowitz, M. (2009) Electroencephalogram theta/beta ratio and arousal in attention-deficit/hyperactivity disorder: evidence of independent processes. *Biol Psychiatry* **66,** 398-401.

Barry, R. J., Johnstone, S. J. and Clarke, A. R. (2003) A review of electrophysiology in attention-deficit/hyperactivity disorder: II. Event-related potentials. *Clin Neurophysiol* **114,** 184-198.

Bear, M. F., Huber, K. M. and Warren, S. T. (2004) The mGluR theory of fragile X mental retardation. *Trends in Neurosciences* **27,** 370-377.

Bernardet, M. and Crusio, W. E. (2006) Fmr1 KO mice as a possible model of autistic features. *ScientificWorldJournal* **6,** 1164-1176.

Bhattacharya, A., Kaphzan, H., Alvarez-Dieppa, A. C., Murphy, J. P., Pierre, P. and Klann, E. (2012) Genetic removal of p70 S6 kinase 1 corrects molecular, synaptic, and behavioral phenotypes in fragile X syndrome mice. *Neuron* **76,** 325-337.

Bilousova, T. V., Dansie, L., Ngo, M., Aye, J., Charles, J. R., Ethell, D. W. and Ethell, I. M. (2009) Minocycline promotes dendritic spine maturation and improves behavioural performance in the fragile X mouse model. *J Med Genet* **46,** 94-102.

Born, H. A., Dao, A. T., Levine, A. T., Lee, W. L., Mehta, N. M., Mehra, S., Weeber, E. J. and Anderson, A. E. (2017) Strain-dependence of the Angelman Syndrome phenotypes in Ube3a maternal deficiency mice. *Sci Rep* **7,** 8451.

Brown, S., Bernardo, M. M., Li, Z. H., Kotra, L. P., Tanaka, Y., Fridman, R. and Mobashery, S. (2000) Potent and selective mechanism-based inhibition of gelatinases. *Journal of the American Chemical Society* **122,** 6799-6800.

Busquets-Garcia, A., Maldonado, R. and Ozaita, A. (2014) New insights into the molecular pathophysiology of fragile X syndrome and therapeutic perspectives from the animal model. *Int J Biochem Cell Biol* **53,** 121-126.

Buzsaki, G. and Wang, X. J. (2012) Mechanisms of gamma oscillations. *Annu Rev Neurosci* **35,** 203-225.

Castren, M., Paakkonen, A., Tarkka, I. M., Ryynanen, M. and Partanen, J. (2003) Augmentation of auditory N1 in children with fragile X syndrome. *Brain Topogr* **15,** 165-171.

Castren, M. L. and Castren, E. (2014) BDNF in fragile X syndrome. *Neuropharmacology* **76 Pt C,** 729-736.

Cellerino, A., Maffei, L. and Domenici, L. (1996) The distribution of brain-derived neurotrophic factor and its receptor trkB in parvalbumin-containing neurons of the rat visual cortex. *Eur J Neurosci* **8,** 1190-1197.

Chu, P., Abraham, R., Budhu, K., Khan, U., De Marco Garcia, N. and Brumberg, J. C. (2018) The Impact of Perineuronal Net Digestion Using Chondroitinase ABC on the Intrinsic Physiology of Cortical Neurons. *Neuroscience* **388,** 23-35.

Contractor, A., Klyachko, V. A. and Portera-Cailliau, C. (2015) Altered Neuronal and Circuit Excitability in Fragile X Syndrome. *Neuron* **87,** 699-715.

Crane, L., Goddard, L. and Pring, L. (2009) Sensory processing in adults with autism spectrum disorders. *Autism* **13,** 215-228.

Crawford, D. C., Acuna, J. M. and Sherman, S. L. (2001) FMR1 and the fragile X syndrome: human genome epidemiology review. *Genet Med* **3,** 359-371.

Dansie, L. E., Phommahaxay, K., Okusanya, A. G., Uwadia, J., Huang, M., Rotschafer, S. E., Razak, K. A., Ethell, D. W. and Ethell, I. M. (2013) Long-lasting effects of minocycline on behavior in young but not adult Fragile X mice. *Neuroscience* **246,** 186-198.

Ding, Q., Sethna, F. and Wang, H. (2014) Behavioral analysis of male and female Fmr1 knockout mice on C57BL/6 background. *Behav Brain Res* **271,** 72-78.

Dvorak, D. and Fenton, A. A. (2014) On track with two gammas. *Neuron* **82,** 506-508.

Dziembowska, M., Pretto, D. I., Janusz, A., Kaczmarek, L., Leigh, M. J., Gabriel, N., Durbin-Johnson, B., Hagerman, R. J. and Tassone, F. (2013) High MMP-9 activity levels in fragile X syndrome are lowered by minocycline. *Am J Med Genet A* **161A,** 1897-1903.

Ethridge, L. E., De Stefano, L. A., Schmitt, L. M. et al. (2019) Auditory EEG Biomarkers in Fragile X Syndrome: Clinical Relevance. *Front Integr Neurosci* **13,** 60.

Ethridge, L. E., White, S. P., Mosconi, M. W., Wang, J., Byerly, M. J. and Sweeney, J. A. (2016) Reduced habituation of auditory evoked potentials indicate cortical hyper-excitability in Fragile X Syndrome. *Transl Psychiatry* **6,** e787.

Ethridge, L. E., White, S. P., Mosconi, M. W., Wang, J., Pedapati, E. V., Erickson, C. A., Byerly, M. J. and Sweeney, J. A. (2017) Neural synchronization deficits linked to cortical hyper-excitability and auditory hypersensitivity in fragile X syndrome. *Mol Autism* **8,** 22.

Filice, F., Vorckel, K. J., Sungur, A. O., Wohr, M. and Schwaller, B. (2016) Reduction in parvalbumin expression not loss of the parvalbumin-expressing GABA interneuron subpopulation in genetic parvalbumin and shank mouse models of autism. *Mol Brain* **9,** 10.

Gibson, J. R., Bartley, A. F., Hays, S. A. and Huber, K. M. (2008) Imbalance of neocortical excitation and inhibition and altered UP states reflect network hyperexcitability in the mouse model of fragile X syndrome. *J Neurophysiol* **100,** 2615-2626.

Gkogkas, C. G., Khoutorsky, A., Cao, R. et al. (2014) Pharmacogenetic inhibition of eIF4E-dependent Mmp9 mRNA translation reverses fragile X syndrome-like phenotypes. *Cell Rep* **9,** 1742-1755.

Goel, A., Cantu, D. A., Guilfoyle, J. et al. (2018) Impaired perceptual learning in a mouse model of Fragile X syndrome is mediated by parvalbumin neuron dysfunction and is reversible. *Nat Neurosci* **21,** 1404-1411.

Gooyit, M., Suckow, M. A., Schroeder, V. A., Wolter, W. R., Mobashery, S. and Chang, M. (2012) Selective gelatinase inhibitor neuroprotective agents cross the blood-brain barrier. *ACS Chem Neurosci* **3,** 730-736.

Hagerman, R. J., Rivera, S. M. and Hagerman, P. J. (2008) The Fragile X Family of Disorders: A Model for Autism and Targeted Treatments. *Current Pediatric Reviews* **4,** 40-52.

Hong, E. J., McCord, A. E. and Greenberg, M. E. (2008) A biological function for the neuronal activity-dependent component of Bdnf transcription in the development of cortical inhibition. *Neuron* **60,** 610-624.

Huber, K. M. (2002) Altered synaptic plasticity in a mouse model of fragile X mental retardation. *Pro Natl Acad Sci USA* **99,** 7746-7750.

Itami, C., Kimura, F. and Nakamura, S. (2007) Brain-derived neurotrophic factor regulates the maturation of layer 4 fast-spiking cells after the second postnatal week in the developing barrel cortex. *J Neurosci* **27,** 2241-2252.

Jensen, O. and Mazaheri, A. (2010) Shaping functional architecture by oscillatory alpha activity: gating by inhibition. *Front Hum Neurosci* **4,** 186.

Kaufmann, W. E., Cortell, R., Kau, A. S., Bukelis, I., Tierney, E., Gray, R. M., Cox, C., Capone, G. T. and Stanard, P. (2004) Autism spectrum disorder in fragile X syndrome: communication, social interaction, and specific behaviors. *Am J Med Genet A* **129A,** 225-234.

Kazdoba, T. M., Leach, P. T., Silverman, J. L. and Crawley, J. N. (2014) Modeling fragile X syndrome in the Fmr1 knockout mouse. *Intractable Rare Dis Res* **3,** 118-133.

Kim, H., Gibboni, R., Kirkhart, C. and Bao, S. (2013) Impaired critical period plasticity in primary auditory cortex of fragile X model mice. *J Neurosci* **33,** 15686-15692.

Klann, E. and Dever, T. E. (2004) Biochemical mechanisms for translational regulation in synaptic plasticity. *Nature reviews. Neuroscience* **5,** 931-942.

Klimesch, W. (1999) EEG alpha and theta oscillations reflect cognitive and memory performance: a review and analysis. *Brain Res Brain Res Rev* **29,** 169-195.

Kulinich, A. O., Reinhard, S. M., Rais, M., Lovelace, J. W., Scott, V., Binder, D. K., Razak, K. A. and Ethell, I. M. (2019) Beneficial effects of sound exposure on auditory cortex development in a mouse model of Fragile X Syndrome. *Neurobiol Dis* **134,** 104622.

Laggerbauer, B. (2001) Evidence that fragile X mental retardation protein is a negative regulator of translation. *Human Molecular Genetics* **10,** 329-338.

Lensjo, K. K., Christensen, A. C., Tennoe, S., Fyhn, M. and Hafting, T. (2017) Differential Expression and Cell-Type Specificity of Perineuronal Nets in Hippocampus, Medial Entorhinal Cortex, and Visual Cortex Examined in the Rat and Mouse. *eNeuro* **4**.

Lewis, D. A., Hashimoto, T. and Volk, D. W. (2005) Cortical inhibitory neurons and schizophrenia. *Nature reviews. Neuroscience* **6,** 312-324.

Lovelace, J. W., Ethell, I. M., Binder, D. K. and Razak, K. A. (2018) Translation-relevant EEG phenotypes in a mouse model of Fragile X Syndrome. *Neurobiol Dis* **115,** 39-48.

Lovelace, J. W., Rais, M., Palacios, A. R. et al. (2019) Deletion of Fmr1 from Forebrain Excitatory Neurons Triggers Abnormal Cellular, EEG, and Behavioral Phenotypes in the Auditory Cortex of a Mouse Model of Fragile X Syndrome. *Cereb Cortex*.

Lovelace, J. W., Wen, T. H., Reinhard, S., Hsu, M. S., Sidhu, H., Ethell, I. M., Binder, D. K. and Razak, K. A. (2016) Matrix metalloproteinase-9 deletion rescues auditory evoked potential habituation deficit in a mouse model of Fragile X Syndrome. *Neurobiol Dis* **89,** 126-135.

Maris, E. and Oostenveld, R. (2007) Nonparametric statistical testing of EEG- and MEG-data. *J Neurosci Methods* **164,** 177-190.

Martin del Campo, H. N., Measor, K. R. and Razak, K. A. (2012) Parvalbumin immunoreactivity in the auditory cortex of a mouse model of presbycusis. *Hear Res* **294,** 31-39.

Mathewson, K. E., Lleras, A., Beck, D. M., Fabiani, M., Ro, T. and Gratton, G. (2011) Pulsed out of awareness: EEG alpha oscillations represent a pulsed-inhibition of ongoing cortical processing. *Front Psychol* **2,** 99.

McDiarmid, T. A., Bernardos, A. C. and Rankin, C. H. (2017) Habituation is altered in neuropsychiatric disorders-a comprehensive review with recommendations for experimental design and analysis. *Neurosci Biobehav Rev* **80,** 286-305.

Miller, L. J., McIntosh, D. N., McGrath, J. et al. (1999) Electrodermal responses to sensory stimuli in individuals with fragile X syndrome: a preliminary report. *Am J Med Genet* **83,** 268-279.

Niell, C. M. and Stryker, M. P. (2010) Modulation of visual responses by behavioral state in mouse visual cortex. *Neuron* **65,** 472-479.

Nomura, T., Musial, T. F., Marshall, J. J., Zhu, Y., Remmers, C. L., Xu, J., Nicholson, D. A. and Contractor, A. (2017) Delayed Maturation of Fast-Spiking Interneurons Is Rectified by Activation of the TrkB Receptor in the Mouse Model of Fragile X Syndrome. *J Neurosci* **37,** 11298-11310.

Oswald, A. M. and Reyes, A. D. (2008) Maturation of intrinsic and synaptic properties of layer 2/3 pyramidal neurons in mouse auditory cortex. *J Neurophysiol* **99,** 2998-3008.

Paluszkiewicz, S. M., Olmos-Serrano, J. L., Corbin, J. G. and Huntsman, M. M. (2011) Impaired inhibitory control of cortical synchronization in fragile X syndrome. *J Neurophysiol* **106,** 2264-2272.

Perez-Alcazar, M., Nicolas, M. J., Valencia, M., Alegre, M., Iriarte, J. and Artieda, J. (2008) Chirp-evoked potentials in the awake and anesthetized rat. A procedure to assess changes in cortical oscillatory activity. *Exp Neurol* **210,** 144-153.

Purcell, D. W., John, S. M., Schneider, B. A. and Picton, T. W. (2004) Human temporal auditory acuity as assessed by envelope following responses. *J Acoust Soc Am* **116,** 3581-3593.

Radwan, B., Dvorak, D. and Fenton, A. A. (2016) Impaired cognitive discrimination and discoordination of coupled theta-gamma oscillations in Fmr1 knockout mice. *Neurobiol Dis* **88,** 125-138.

Rais, M., Binder, D. K., Razak, K. A. and Ethell, I. M. (2018) Sensory Processing Phenotypes in Fragile X Syndrome. *ASN Neuro* **10,** 1759091418801092.

Ray, S. and Maunsell, J. H. (2011) Different origins of gamma rhythm and high-gamma activity in macaque visual cortex. *PLoS Biol* **9,** e1000610.

Rotschafer, S. and Razak, K. (2013) Altered auditory processing in a mouse model of fragile X syndrome. *Brain Res* **1506,** 12-24.

Schneider, A., Leigh, M. J., Adams, P., Nanakul, R., Chechi, T., Olichney, J., Hagerman, R. and Hessl, D. (2013) Electrocortical changes associated with minocycline treatment in fragile X syndrome. *J Psychopharmacol* **27,** 956-963.

Selby, L., Zhang, C. and Sun, Q. Q. (2007) Major defects in neocortical GABAergic inhibitory circuits in mice lacking the fragile X mental retardation protein. *Neurosci Lett* **412,** 227-232.

Sharma, A., Hoeffer, C. A., Takayasu, Y., Miyawaki, T., McBride, S. M., Klann, E. and Zukin, R. S. (2010) Dysregulation of mTOR Signaling in Fragile X Syndrome. *J Neurosci* **30,** 694-702.

Sidhu, H., Dansie, L. E., Hickmott, P. W., Ethell, D. W. and Ethell, I. M. (2014) Genetic removal of matrix metalloproteinase 9 rescues the symptoms of fragile X syndrome in a mouse model. *J Neurosci* **34,** 9867-9879.

Siller, S. S. and Broadie, K. (2011) Neural circuit architecture defects in a Drosophila model of Fragile X syndrome are alleviated by minocycline treatment and genetic removal of matrix metalloproteinase. *Dis Model Mech* **4,** 673-685.

Sinclair, D., Oranje, B., Razak, K. A., Siegel, S. J. and Schmid, S. (2017) Sensory processing in autism spectrum disorders and Fragile X syndrome-From the clinic to animal models. *Neurosci Biobehav Rev* **76,** 235-253.

Sohal, V. S., Zhang, F., Yizhar, O. and Deisseroth, K. (2009) Parvalbumin neurons and gamma rhythms enhance cortical circuit performance. *Nature* **459,** 698-702.

Talisa, V. B., Boyle, L., Crafa, D. and Kaufmann, W. E. (2014) Autism and anxiety in males with fragile X syndrome: an exploratory analysis of neurobehavioral profiles from a parent survey. *Am J Med Genet A* **164A,** 1198-1203.

Tallon-Baudry, C., Bertrand, O., Delpuech, C. and Pernier, J. (1996) Stimulus specificity of phase-locked and non-phase-locked 40 Hz visual responses in human. *J Neurosci* **16,** 4240-4249.

Toledo, M. A., Wen, T. H., Binder, D. K., Ethell, I. M. and Razak, K. A. (2019) Reversal of ultrasonic vocalization deficits in a mouse model of Fragile X Syndrome with minocycline treatment or genetic reduction of MMP-9. *Behav Brain Res* **372,** 112068.

Troca-Marin, J. A., Alves-Sampaio, A. and Montesinos, M. L. (2012) Deregulated mTOR-mediated translation in intellectual disability. *Prog Neurobiol* **96,** 268-282.

Van der Molen, M. J. and Van der Molen, M. W. (2013) Reduced alpha and exaggerated theta power during the resting-state EEG in fragile X syndrome. *Biol Psychol* **92,** 216-219.

Vandooren, J., Geurts, N., Martens, E., Van den Steen, P. E., Jonghe, S. D., Herdewijn, P. and Opdenakker, G. (2011) Gelatin degradation assay reveals MMP-9 inhibitors and function of O-glycosylated domain. *World J Biol Chem* **2,** 14-24.

Verkerk, A. J., Pieretti, M., Sutcliffe, J. S. et al. (1991) Identification of a gene (FMR-1) containing a CGG repeat coincident with a breakpoint cluster region exhibiting length variation in fragile X syndrome. *Cell* **65,** 905-914.

Vreugdenhil, M., Jefferys, J. G., Celio, M. R. and Schwaller, B. (2003) Parvalbumin-deficiency facilitates repetitive IPSCs and gamma oscillations in the hippocampus. *J Neurophysiol* **89,** 1414-1422.

Wang, J., Barstein, J., Ethridge, L. E., Mosconi, M. W., Takarae, Y. and Sweeney, J. A. (2013) Resting state EEG abnormalities in autism spectrum disorders. *J Neurodev Disord* **5,** 24.

Wang, J., Ethridge, L. E., Mosconi, M. W., White, S. P., Binder, D. K., Pedapati, E. V., Erickson, C. A., Byerly, M. J. and Sweeney, J. A. (2017) A resting EEG study of neocortical hyperexcitability and altered functional connectivity in fragile X syndrome. *J Neurodev Disord* **9,** 11.

Wen, T. H., Afroz, S., Reinhard, S. M., Palacios, A. R., Tapia, K., Binder, D. K., Razak, K. A. and Ethell, I. M. (2018) Genetic Reduction of Matrix Metalloproteinase-9 Promotes Formation of Perineuronal Nets Around Parvalbumin-Expressing Interneurons and Normalizes Auditory Cortex Responses in Developing Fmr1 Knock-Out Mice. *Cereb Cortex* **28,** 3951-3964.

Wen, T. H., Lovelace, J. W., Ethell, I. M., Binder, D. K. and Razak, K. A. (2019) Developmental Changes in EEG Phenotypes in a Mouse Model of Fragile X Syndrome. *Neuroscience* **398,** 126-143.

Woo, C. C. and Leon, M. (2013) Environmental enrichment as an effective treatment for autism: a randomized controlled trial. *Behav Neurosci* **127,** 487-497.

Xenos, D., Kamceva, M., Tomasi, S., Cardin, J. A., Schwartz, M. L. and Vaccarino, F. M. (2018) Loss of TrkB Signaling in Parvalbumin-Expressing Basket Cells Results in Network Activity Disruption and Abnormal Behavior. *Cereb Cortex* **28,** 3399-3413.

Yamada, J., Ohgomori, T. and Jinno, S. (2015) Perineuronal nets affect parvalbumin expression in GABAergic neurons of the mouse hippocampus. *Eur J Neurosci* **41,** 368-378.

Yan, Q. J., Asafo-Adjei, P. K., Arnold, H. M., Brown, R. E. and Bauchwitz, R. P. (2004) A phenotypic and molecular characterization of the fmr1-tm1Cgr fragile X mouse. *Genes Brain Behav* **3,** 337-359.

Yan, Q. J., Rammal, M., Tranfaglia, M. and Bauchwitz, R. P. (2005) Suppression of two major Fragile X Syndrome mouse model phenotypes by the mGluR5 antagonist MPEP. *Neuropharmacology* **49,** 1053-1066.

Zheng, K., An, J. J., Yang, F. et al. (2011) TrkB signaling in parvalbumin-positive interneurons is critical for gamma-band network synchronization in hippocampus. *Pro Natl Acad Sci USA* **108,** 17201-17206.

Figure Legends

Figure 1. Developing *Fmr1* KO mice exhibit increased low gamma power. (A) Experimental timeline shows mice were implanted at P18 with 2-channel EEG electrodes (WT, N=35; *Fmr1*

KO, N=30) in the auditory cortex (AC) and the frontal cortex (FC), and with an occipital cortex reference electrode. Animals were allowed four-five days to recover post-surgery (WT, N=35; *Fmr1* KO, N=30; N=14 (WT N=8; KO N=6) animals died post-surgery) and EEG recording was done prior to treatment (PRE) at P22-23 (WT, N=23, excluded N=1; *Fmr1* KO, N=21, excluded N=1). Immediately after the EEG recording, animals were given either an intraperitoneal injection of SB-3CT (25mg/kg) or vehicle. At P23-24, a post treatment EEG recording was performed. Brains were collected for PV/PNN analysis immediately after EEG recording. (B) Schematic shows placement of electrodes, which consisted of a three-channel electrode post with three 1-mm stainless steel screws (depicted by red dots). (C-J) EEG recording was done prior to treatment (PRE) at P22-23. Resting data (baseline, in the absence of auditory stimulation) was collected for five minutes and divided into two-second segments for spectral analysis. Depicted are examples of EEG segments from individual WT (C) and *Fmr1* KO (D) mice, which include simultaneous recording from the AC and the FC. (E-F) Graphs show average spectral power ($\mu V^2/Hz$) in the AC and FC of *Fmr1* KO mice (N=20) in a histogram (E) and bar graph format (F) expressed as the ratio of WT controls (N=22) prior to treatment (PRE). A value of 1 indicates no mean difference in power between WT and *Fmr1* KO mice, while values above the black line indicate KO > WT, and below indicate KO < WT. (F) Statistical analysis was performed using a one-way MANCOVA with the percentage of time spent moving as a covariate. Genotype differences were compared using six spectral bands per region: Delta (D), Theta (T), Alpha, Beta (B), Low Gamma (LG), and High Gamma (HG). Since assumptions were not violated, we report an effect of genotype (AC: Pillai's Trace =2.465, p=0.04; FC: Pillai's Trace = 2.587, p=0.036) across all 6 of the combined frequency variables. Low gamma was significantly increased after correction for multiple comparisons in the both the AC and FC: AC low gamma, F (1,27) =10,

p=0.003, η^2=0.204, FC low gamma, F (1,27) =9.012, p=0.005, η^2=0.188 (WT N=22, *Fmr1* KO N=20). All graphs represent average values and the error bars indicate SEM. To determine if there is a relationship between power across different frequencies and/or regions, a Pearson's correlation was done for resting baseline segments comparing *Fmr1* KO (N=21, excluded N=3) *versus* WT control mice (N=23, excluded N=2). (G) Graph shows Pearson's correlation (r) for each mouse for AC Theta/Low Gamma and AC Alpha/Low Gamma (WT, N=21; *Fmr1* KO, N=18; T1G1: p=0.02; A1G1: p=0.008). (H) Graph shows the Pearson's correlation (r) for FC Theta/Low Gamma and FC Alpha/Low Gamma. (I) Graph shows the Pearson's correlation (r) for AC Theta/FC Low Gamma and AC Alpha/FC Low Gamma (T1G2: p=0.03); A1G2: p= 0.04). (J) Graph shows the Pearson's correlation (r) for the FC Theta/AC Low Gamma and FC Alpha/AC Low Gamma (T2G1: p=0.04; A2G1: p=0.03). For power coupling comparisons, animals that moved less than five percent during the resting baseline were excluded from the analysis.

Figure 2. Acute inhibition of MMP-9 activity ameliorates EEG oscillation deficits in *Fmr1* KO mice. Five minutes of resting EEG activity was recorded from WT and *Fmr1* KO mice post treatment at P23-24 (from treatment groups, N=2 from vehicle-treated WT and *Fmr1* KO groups respectively, and N=1 from the SB-3CT-treated *Fmr1* KO group were excluded from resting baseline EEG analysis). FFT calculated spectral power ($\mu V^2/Hz$) for each group is shown as a ratio of a corresponding control group. (A, D) Average power in the AC (top) and FC (bottom) of vehicle-treated *Fmr1* KO (N=14, excluded N=2) compared to vehicle-treated WT (N=18, excluded N=2). (B, E) Average power in the AC and FC of SB-3CT-treated *Fmr1* KO (N=13, excluded N=1) compared to SB-3CT-treated WT (N=15, no excluded animals). (C, F) Average power of SB-3CT-treated *Fmr1* KO compared to vehicle-treated *Fmr1* KO. All graphs represent

average values and the error bars indicate SEM. Delta (D), Theta (T), Alpha, Beta (B), Low Gamma (LG), and High Gamma (HG).

Figure 3. *Fmr1* KO mice are deficient in phase locking to auditory "Up Chirp" stimuli. (A-B) Inter Trial Phase Coherence (ITPC: ability to synchronize oscillations to stimulus frequencies) grand average for WT (N=23) and *Fmr1* KO (N=19) mice in the AC (top) and FC (bottom). EEG oscillations matched the frequency of the chirp and were seen as increased ITPC along a diagonal, from 0 to 2 s and 1-100Hz. (C) ITPC means for WT PRE were subtracted from *Fmr1* KO PRE mice to show the difference between genotypes. Blue areas indicating KO < WT, green areas no difference, and yellow/red KO > WT. Significant clusters ($p<0.025$) are highlighted by bold-lined contours. (D) Graph shows difference in grand average single trial power (STP) or on-going 'background' power during auditory stimulation between WT PRE and *Fmr1* KO mice in AC (top) and FC (bottom).

Figure 4. Acute SB-3CT treatment improves Inter Trial Phase Coherence (ITPC) to auditory "Up Chirp" stimuli in *Fmr1* KO mice. (A, B) Grand average ITPC in AC and FC of vehicle-treated *Fmr1* KO (A, N=12) and SB-3CT-treated *Fmr1* KO (B, N=12). Warmer colors, yellow/red, represent high ITPC values, while cooler colors, blue/green, represent low ITPC values. Significant clusters ($p<0.025$) are highlighted by bold-lined contours. (C) Graph shows the difference in ITPC values between vehicle-treated *Fmr1* KO (N=12) and vehicle-treated WT (N=17). (D) Graph shows the difference in ITPC values between SB-3CT-treated *Fmr1* KO (N=12) and vehicle-treated *Fmr1* KO (N=12).

Figure 5. Acute SB-3CT treatment enhances PNN formation around PV cells in layer 4 auditory cortex of *Fmr1* KO mice. Confocal images of PV immunoreactivity (red; A, E, I, M), PNN labeling with WFA (green; B, F, J, N) and PV/PNN double labeling (C, G, K, O) in

vehicle-treated WT (A-D), SB-3CT-treated WT (E-H), vehicle-treated *Fmr1* KO (I-L), and SB-3CT-treated *Fmr1* KO (M-P). Scale bar, 150 µm. (B) High magnification images of PV/PNN in vehicle-treated WT (D), SB-3CT-treated WT (H), vehicle-treated *Fmr1* KO (L), and SB-3CT-treated *Fmr1* KO (P). Scale bar, 50 µm. (Q-T) Graphs show density of PV cells (Q), PNN-positive cells (R), PV/PNN co-localization (S) and PV-negative cells with PNN (T). All graphs represent average values and the error bars indicate SEM (n=17-23 per group, N=6 per group; *p<0.05; **p<0.01; ***p<0.001; ****p<0.0001).

Figure 6. Acute SB-3CT-treatment normalizes anxiety/hyperactivity phenotype associated with *Fmr1* KO mice. (A) Experimental timeline for behavior and Western blot analysis. For this, mice were given either an intraperitoneal injection of SB-3CT (25mg/kg) or vehicle at P27-28 and were tested for anxiety, locomotor, and hyperactivity using the open field and elevated plus maze test one-day post treatment. Brain samples were collected for Western blot analysis immediately after behavior. (B-D) Graphs show the percent time spent in the open arms (B), total entries into open and closed arms (C), and the average speed (D) in the elevated plus maze. (E-I) Graphs show the total number of center entries (E), the percent time spent in thigmotaxis (F), the time spent in the center per entry (G), the total number of line crosses (H), and the average speed (I) in the open field test. All graphs represent average values and the error bars indicate SEM (WT vs *Fmr1* KO: *p<0.05, **p < 0.01, ****p < 0.0001; vehicle-treated vs SB-3CT-treated *Fmr1* KO: #p<0.05, ##p<0.01, ###p<0.001, ####p<0.0001, vehicle-treated WT, N=10; SB-3CT-treated WT, N=8; vehicle-treated *Fmr1* KO, N=10; SB-3CT-treated *Fmr1* KO, N=9).

Figure 7. Acute MMP-9 inhibition reduces gelatinase activity and phosphorylation of Akt, while increasing PV levels and phosphorylation of TrkB in the AC of *Fmr1* KO mice. To

confirm that the MMP-2/9 inhibitor, SB-3CT, reduced MMP-2/9 activity following treatment, gelatinase activity was measured using a Dye-Quenched (DQ) gelatin assay. (A) Experimental timeline for DQ gelatin assay. Mice (no EEG) were given either an intraperitoneal injection of SB-3CT (25mg/kg) or vehicle at P21-22 and brains were collected for the DQ Gelatin assay one-hour post injection. (B) Graph shows standard curve. (C) *Fmr1* KO mice injected with SB-3CT (25 mg/kg) show reduced gelatinase activity compared to vehicle-treated mice 1 h post injection (N=5 per group, t-test, p=0.02). (D-G) Western blots show levels of pAkt and Akt (D), PV and actin (E), pTrkBY515 (F) and TrkB (D). Graphs show pAkt/Akt (D), PV/actin (E), pTrkBY515/TrkB (F), and TrkB/actin (G) ratios in the AC of vehicle-treated and SB-3CT-treated *Fmr1* KO mice (N=4 per group) 24 h post injection. All graphs represent average values and error bars indicate SEM (*p<0.05).

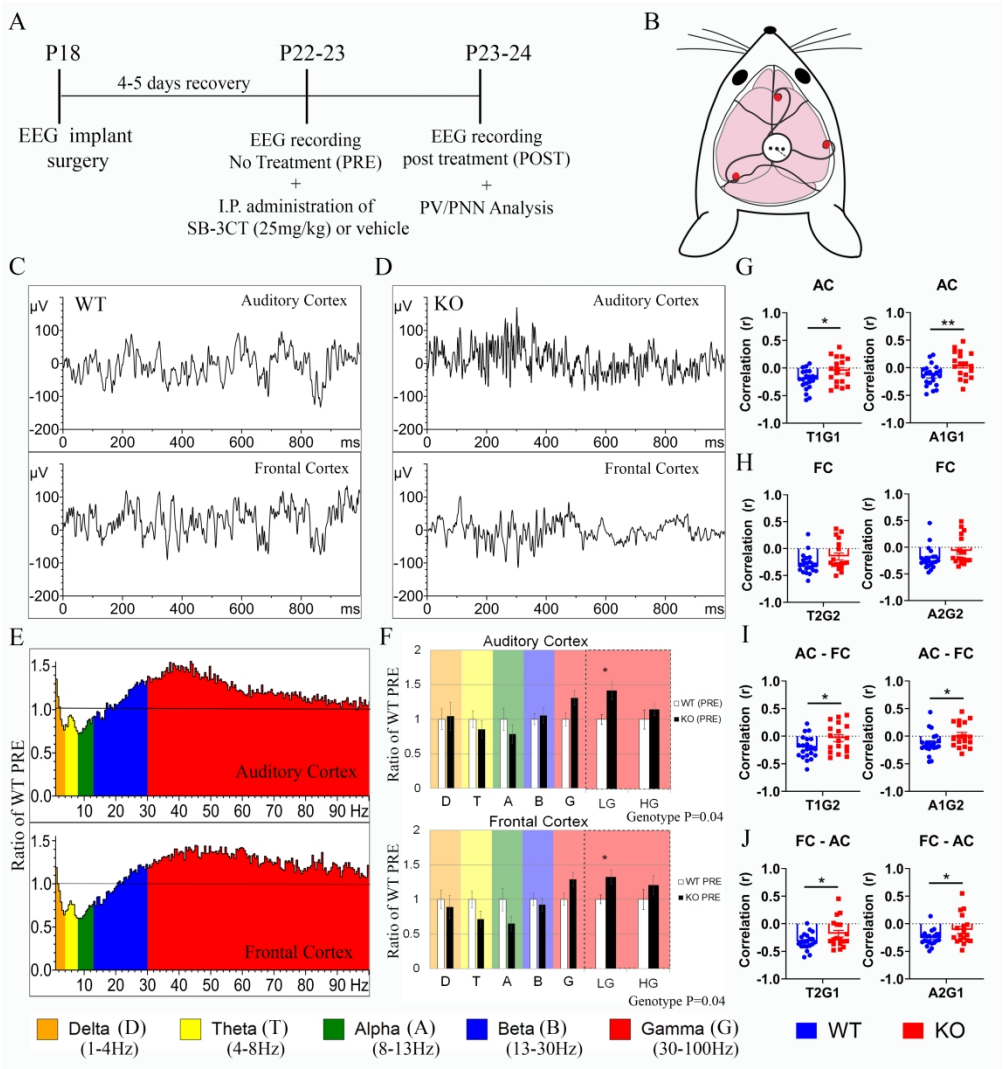

Figure 1. Developing Fmr1 KO mice exhibit increased low gamma power.

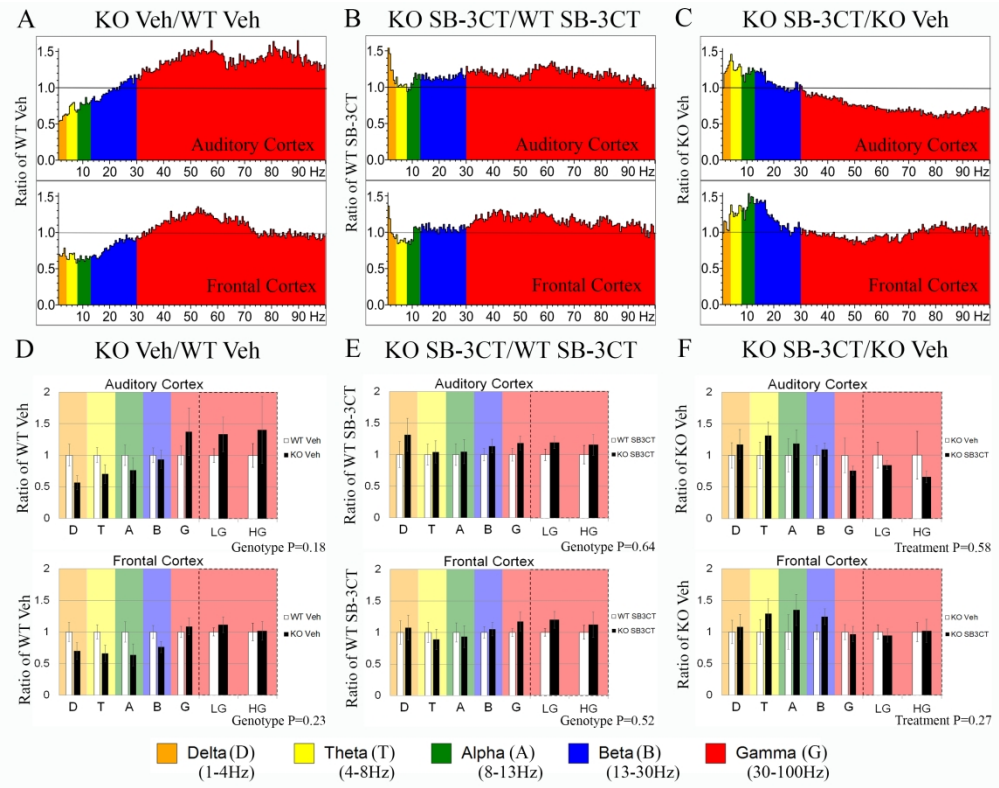

Figure 2. Acute inhibition of MMP-9 activity ameliorates EEG oscillation deficits in Fmr1 KO mice.

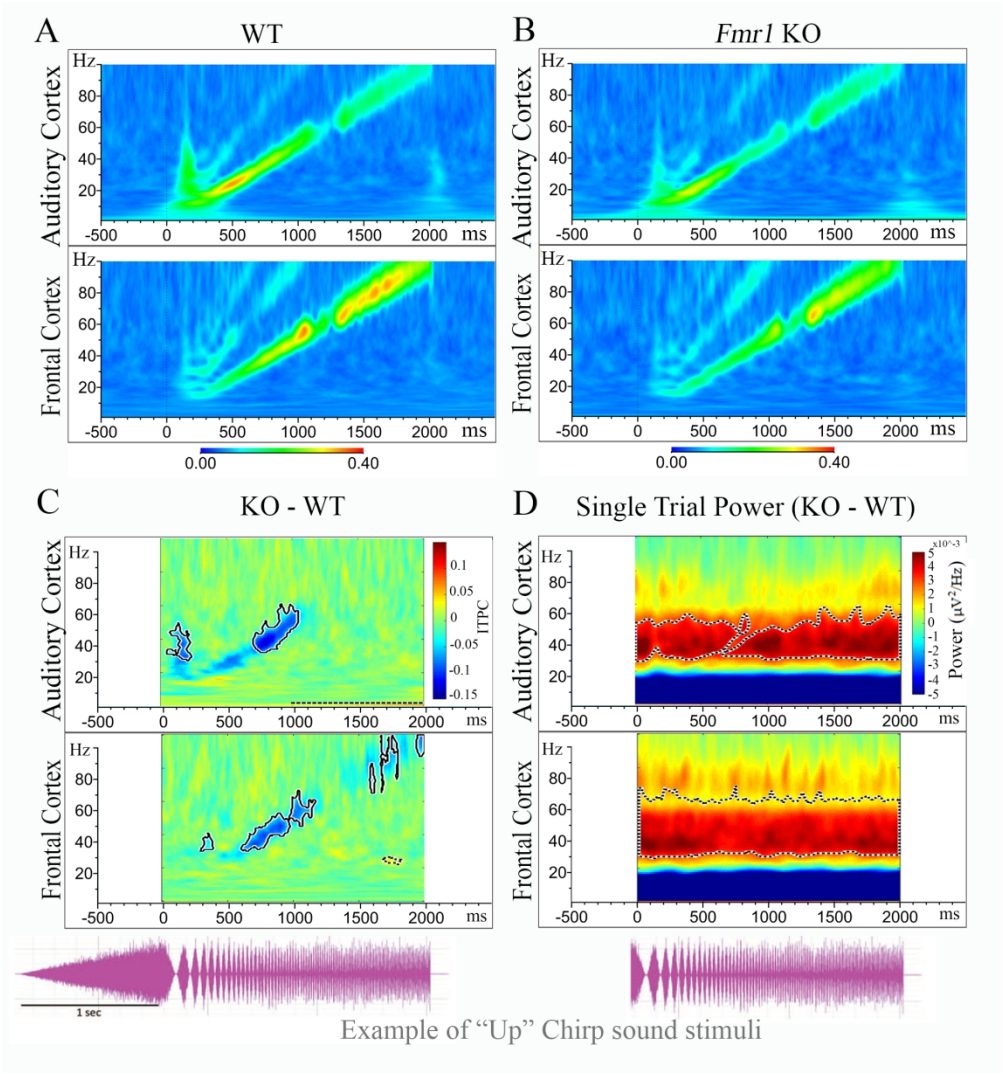

Figure 3. Fmr1 KO mice are deficient in phase locking to auditory "Up Chirp" stimuli.

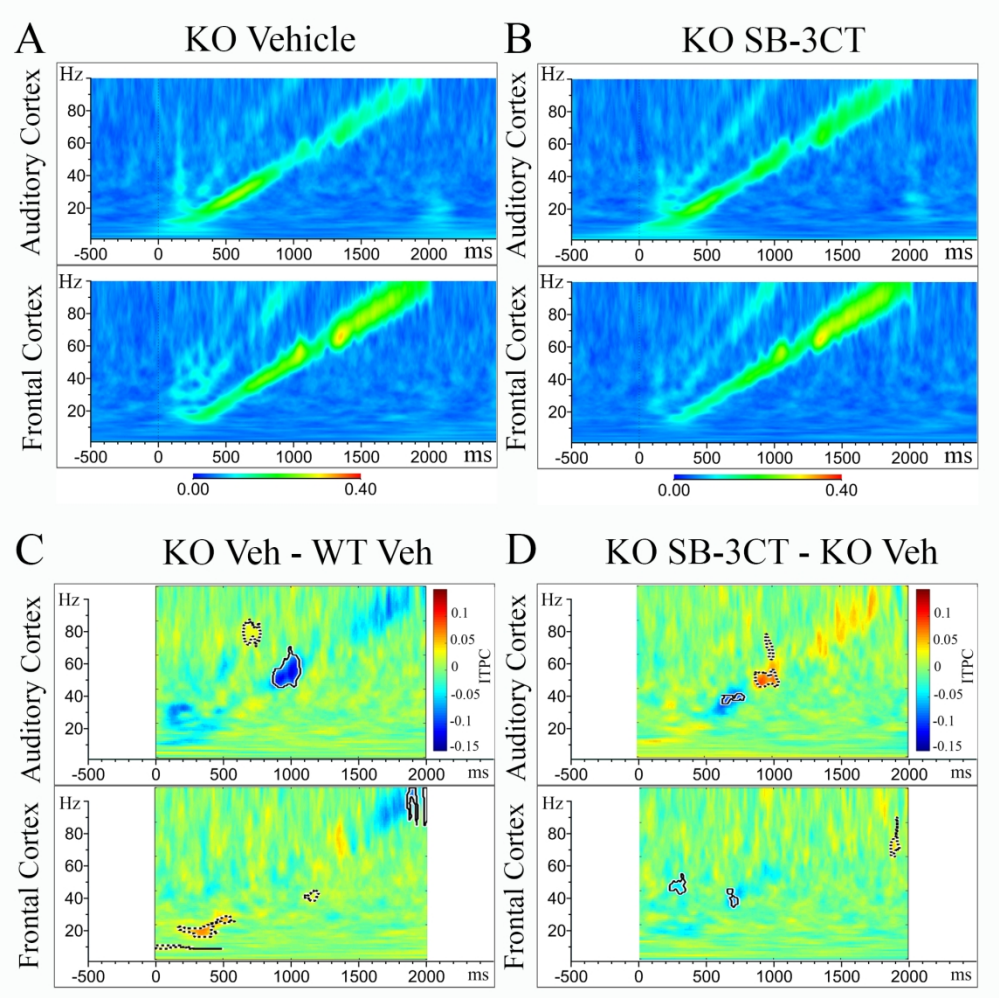

Figure 4. Acute SB-3CT treatment improves Inter Trial Phase Coherence (ITPC) to auditory "Up Chirp" stimuli in Fmr1 KO mice.

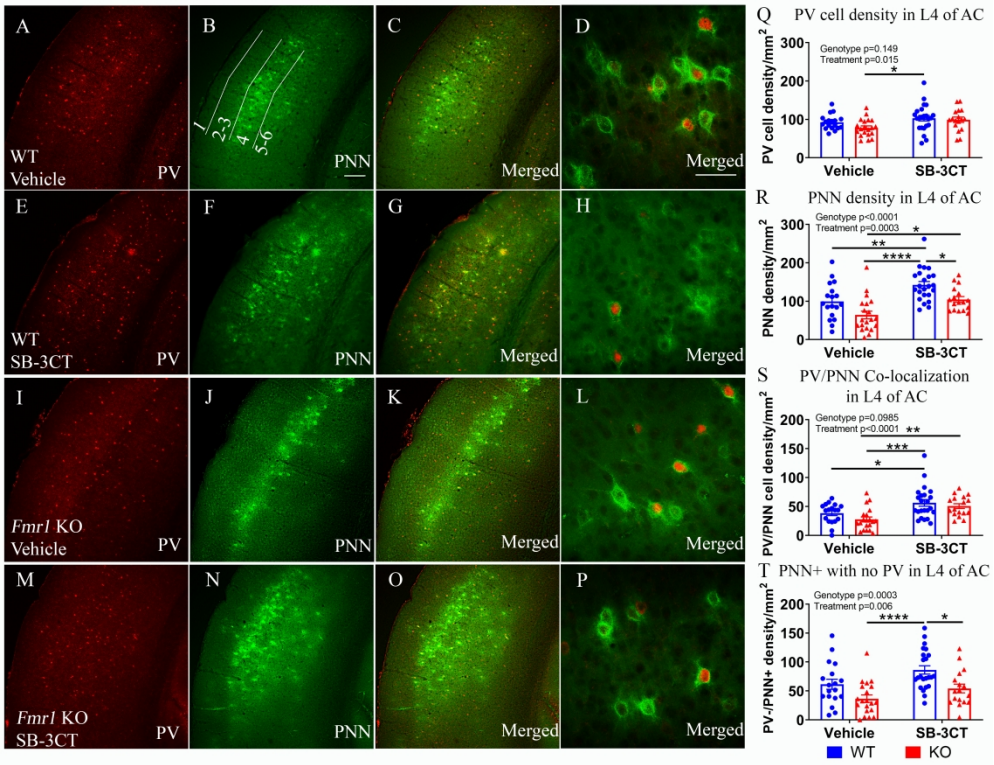

Figure 5. Acute SB-3CT treatment enhances PNN formation around PV cells in layer 4 auditory cortex of Fmr1 KO mice.

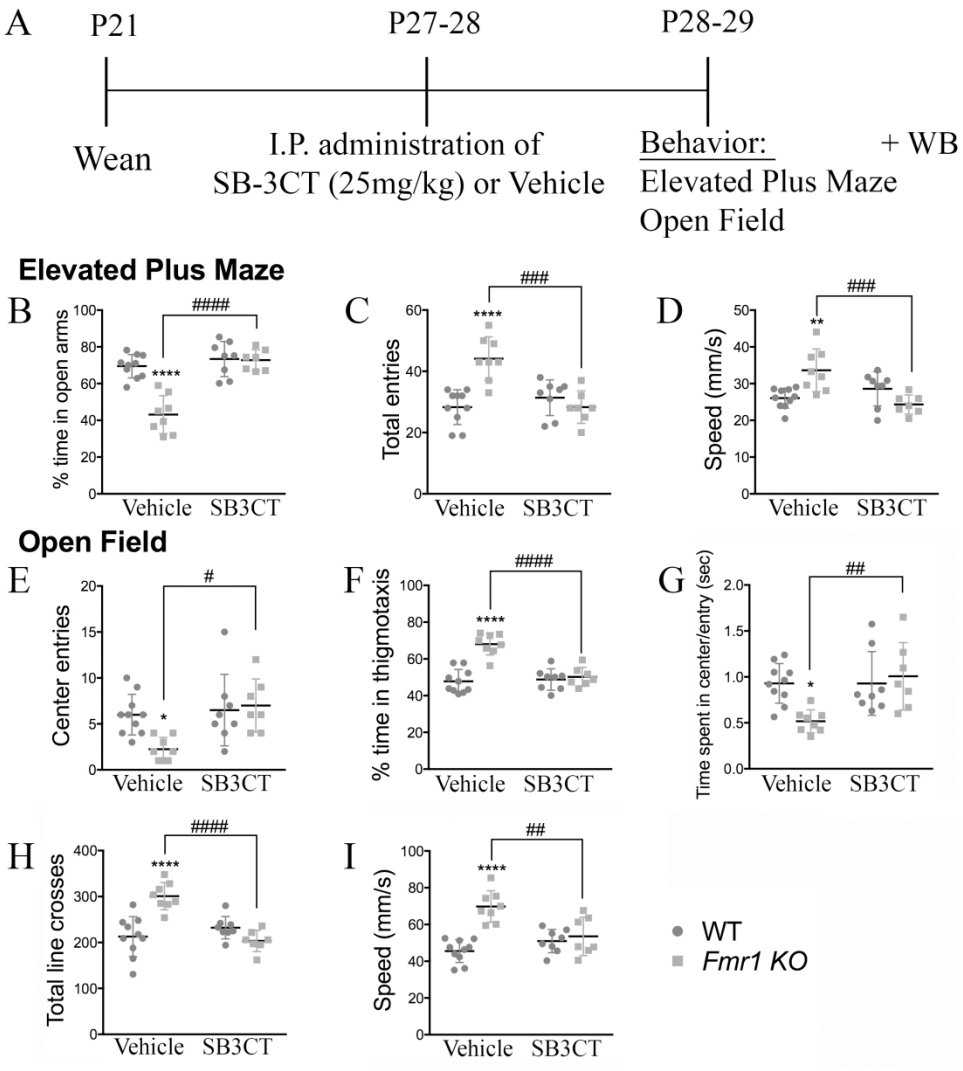

Figure 6. Acute SB-3CT-treatment normalizes anxiety/hyperactivity phenotype associated with Fmr1 KO mice.

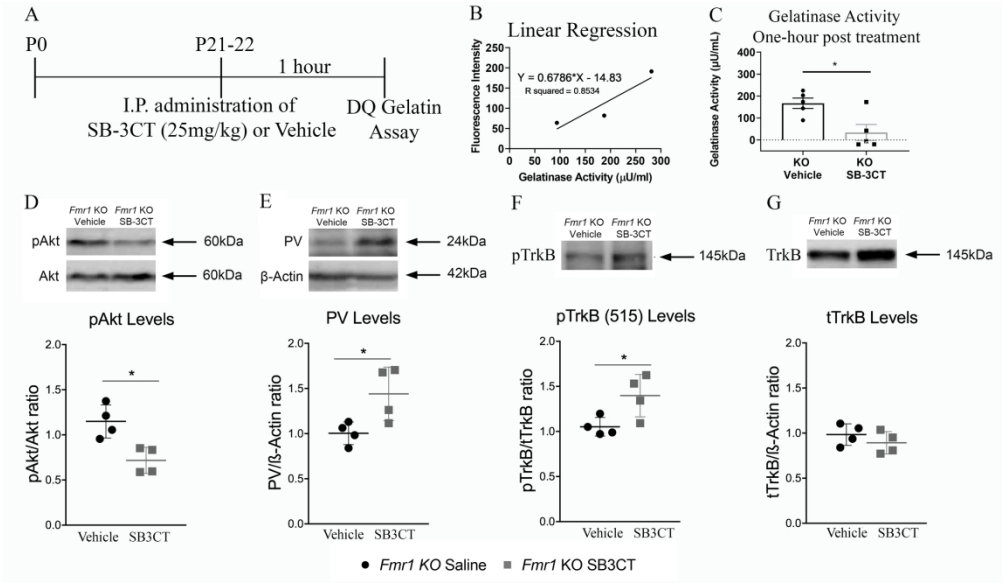

Figure 7. Acute MMP-9 inhibition reduces gelatinase activity and phosphorylation of Akt, while increasing PV levels and phosphorylation of TrkB in the AC of Fmr1 KO mice.

205x119mm (300 x 300 DPI)

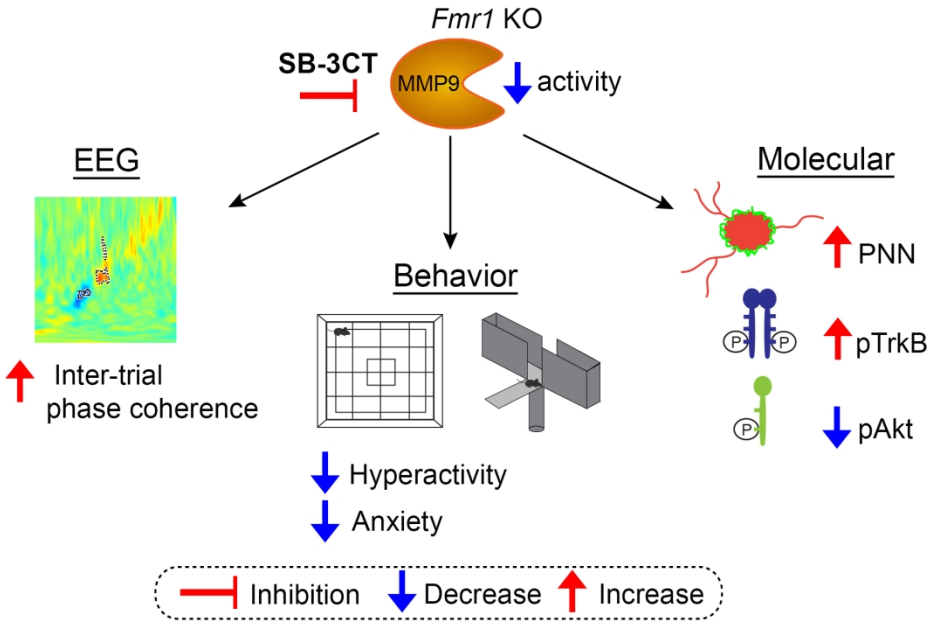
Fmr1 KO
SB-3CT
MMP9
activity
EEG
Molecular
Behavior
PNN
pTrkB
pAkt
Inter-trial
phase coherence
Hyperactivity
Anxiety
Inhibition
Decrease
Increase

Graphical abstract legend

The current study uses the matrix metalloproteinase (MMP)-2/9 inhibitor, SB-3CT, to pharmacologically inhibit MMP-9 activity postnatally to test if acute MMP-9 inhibition reverses neural oscillation deficits, behavioral impairments, and enhances perineuronal net (PNN) formation around parvalbumin (PV) cells in *Fmr1* KO mice. Results show improved evoked synchronization to auditory stimuli and mouse behavior, enhanced PNN formation and TrkB phosphorylation, and reduced aberrant Akt phosphorylation in the auditory cortex of *Fmr1* KO mice. This suggests that MMP-9 inhibition is beneficial in ameliorating cortical processing deficits in FXS and that MMP-9 inhibitors may serve as therapeutic candidates to reduce sensory hypersensitivity.

Acute pharmacological inhibition of matrix metalloproteinase-9 activity during development restores perineuronal net formation and normalizes auditory processing in *Fmr1* KO mice

Patricia S. Pirbhoy[1], Maham Rais[1], Jonathan W. Lovelace[2], Walker Woodard[1], Khaleel A. Razak[2], Devin K. Binder[1], Iryna M. Ethell[1]

[1] Division of Biomedical Sciences, School of Medicine, University of California, Riverside Riverside, California 92521, USA

[2] Department of Psychology, University of California Riverside, Riverside, California 92521, USA

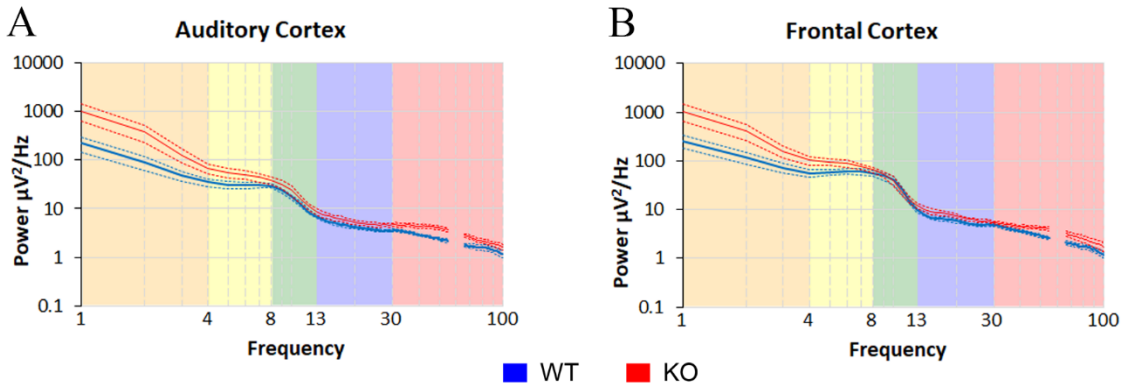

Supplemental Figure 1-1. Characterization of oscillatory EEG patterns in *Fmr1* KO and WT mice. Resting data was collected for 5 min (no auditory stimulus) and was divided into 2-sec segments. Power density (μV^2/Hz) was calculated for each artifact-free segment using Fast Fourier Transforms (FFT) in the auditory and frontal cortex. All segments for a given animal were then averaged and the individual averages then contributed to the genotype averages seen in A and B. Note: frequencies from 55 to 65 Hz were excluded in all analysis, as a 60 Hz notch filter was used to eliminate line noise.

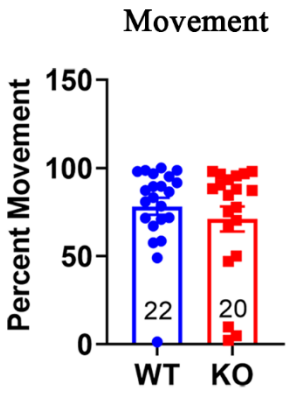

Supplemental Figure 1-2. Percent movement in WT and *Fmr1* KO mice prior to treatment. Percent movement during EEG resting baseline for WT and *Fmr1* KO mice before treatment. Statistical analysis of WT and *Fmr1* KO mice with student's t-test shows no significant difference ($t(40)=0.85$, $p=0.399$)). For EEG power coupling comparisons, animals that moved less than five percent during the resting baseline were excluded from analysis (WT N=1, KO N=2).

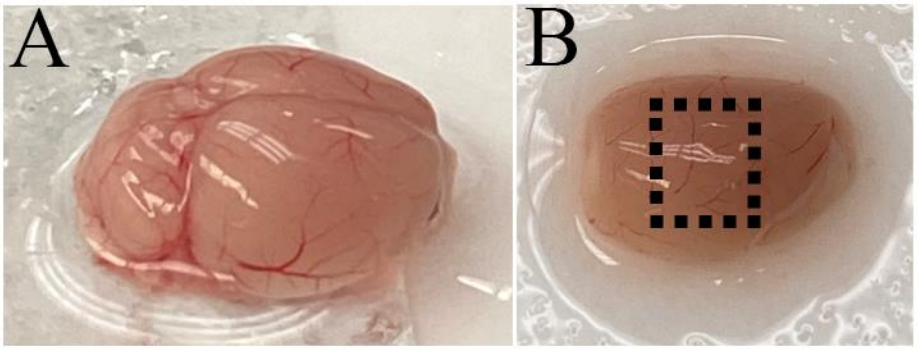

Supplemental Figure 2-1. Dissection of auditory cortex. To dissect out the auditory cortex, the brain was removed and placed on ice-cold PBS with phosphatase and protease inhibitors. The cerebellum was removed, the brain was cut along the sagittal plane to separate the two hemispheres, and the hippocampus was removed. The remaining cortex was cut to isolate the auditory cortex and surrounding cortical structures. Following isolation of cortex, underlying structures were removed.

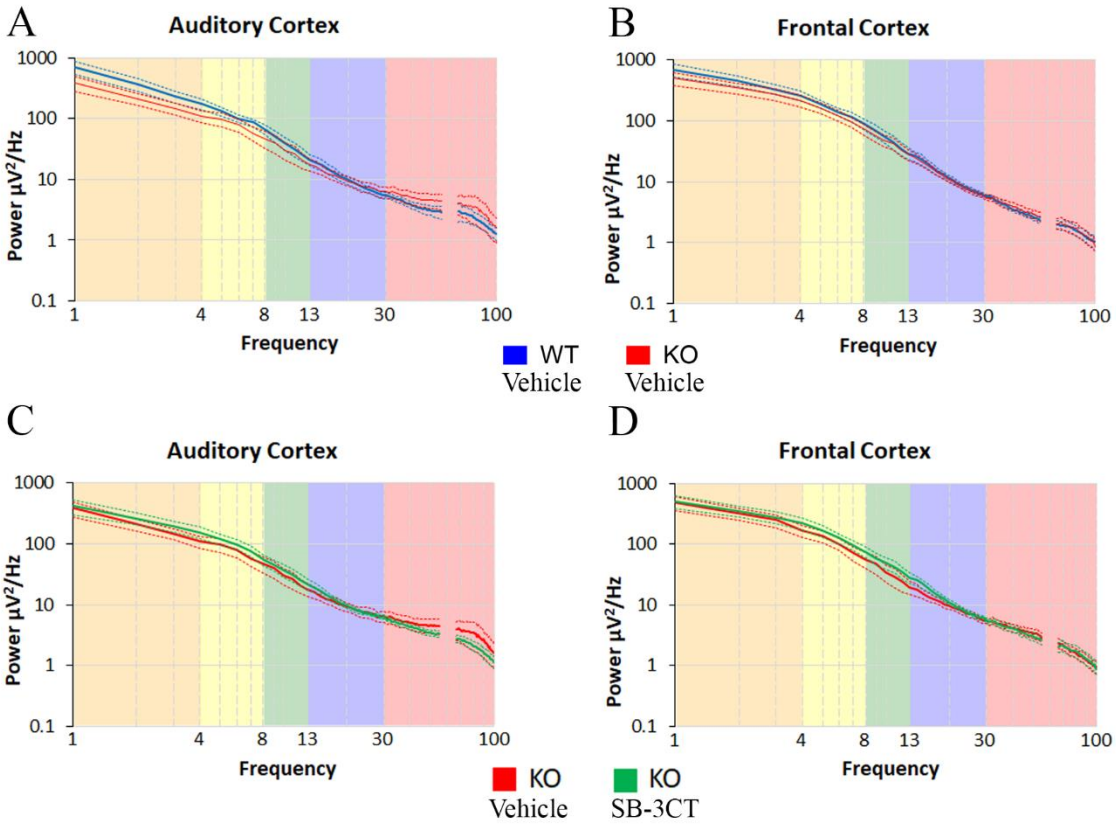

Supplemental Figure 2-2. Characterization of oscillatory EEG patterns in vehicle-treated and SB-3CT-treated *Fmr1* KO and WT mice. Resting data was collected for 5 min (no auditory stimulus) and was divided into 2-sec segments. Power density (μV^2/Hz) was calculated for each artifact-free segment using Fast Fourier Transforms (FFT) in the auditory and frontal cortex. All segments for a given animal were then averaged and the individual averages then contributed to the genotype x treatment averages seen in A-D.

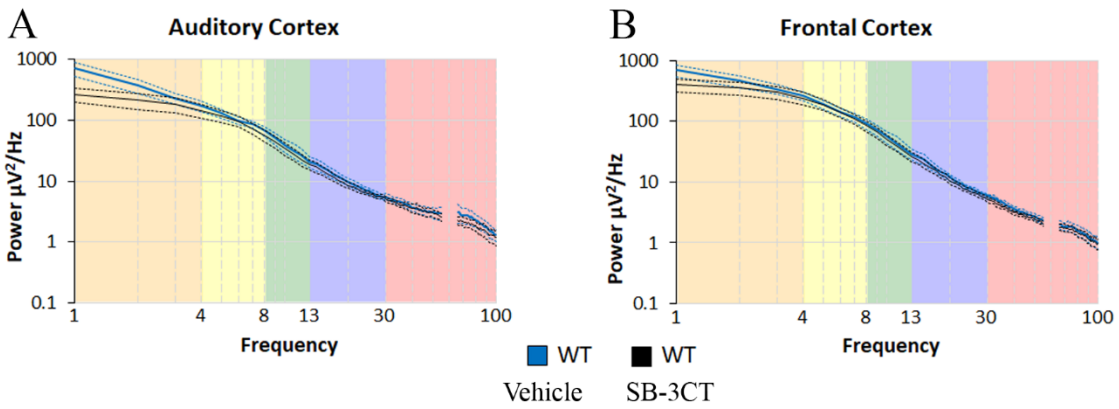

Supplemental Figure 2-3. Characterization of oscillatory EEG patterns in vehicle-treated and SB-3CT-treated WT mice. Resting data was collected for 5 min (no auditory stimulus) and was divided into 2-sec segments. Power density (μV^2/Hz) was calculated for each artifact-free segment using Fast Fourier Transforms (FFT) in the auditory and frontal cortex. All segments for a given animal were then averaged and the individual averages then contributed to the averages seen in A and B.

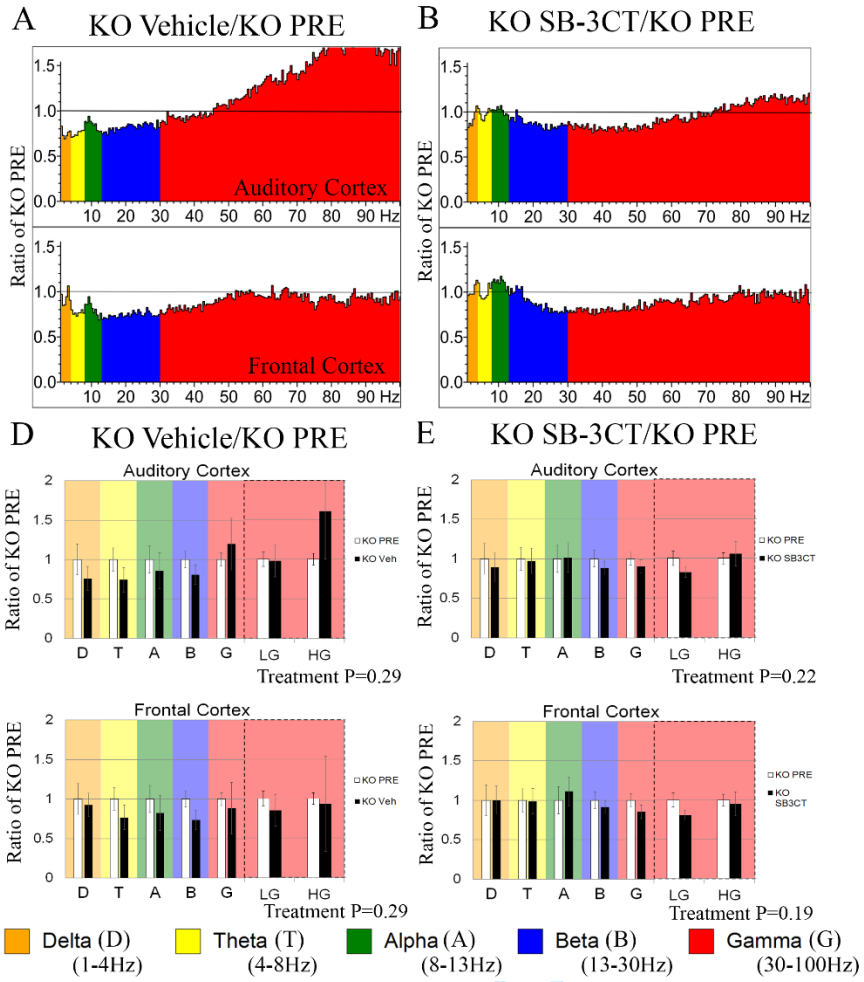

Supplemental Figure 2-4. Comparisons of vehicle- and SB-3CT-treated *Fmr1* KO mice to *Fmr1* KO PRE mice. Five minutes of resting EEG activity was recorded from electrodes implanted in the auditory (AC) and frontal cortex (FC) of vehicle-treated (A) and SB-3CT-treated (B) *Fmr1* KO mice. (D, E) Graphs show FFT calculated spectral power as a ratio of the *Fmr1* KO control group (PRE, N=20) depicted in Figure 1. One-way MANCOVA analysis of *Fmr1* KO comparisons did not reveal any significant differences in any of the frequency bands in both the AC and FC. A value of 1 indicates no mean difference in power between *Fmr1* KO treated and *Fmr1* KO control, while values above the black line indicate *Fmr1* KO treated > *Fmr1* KO control, and below indicates *Fmr1* KO treated < *Fmr1* KO control.

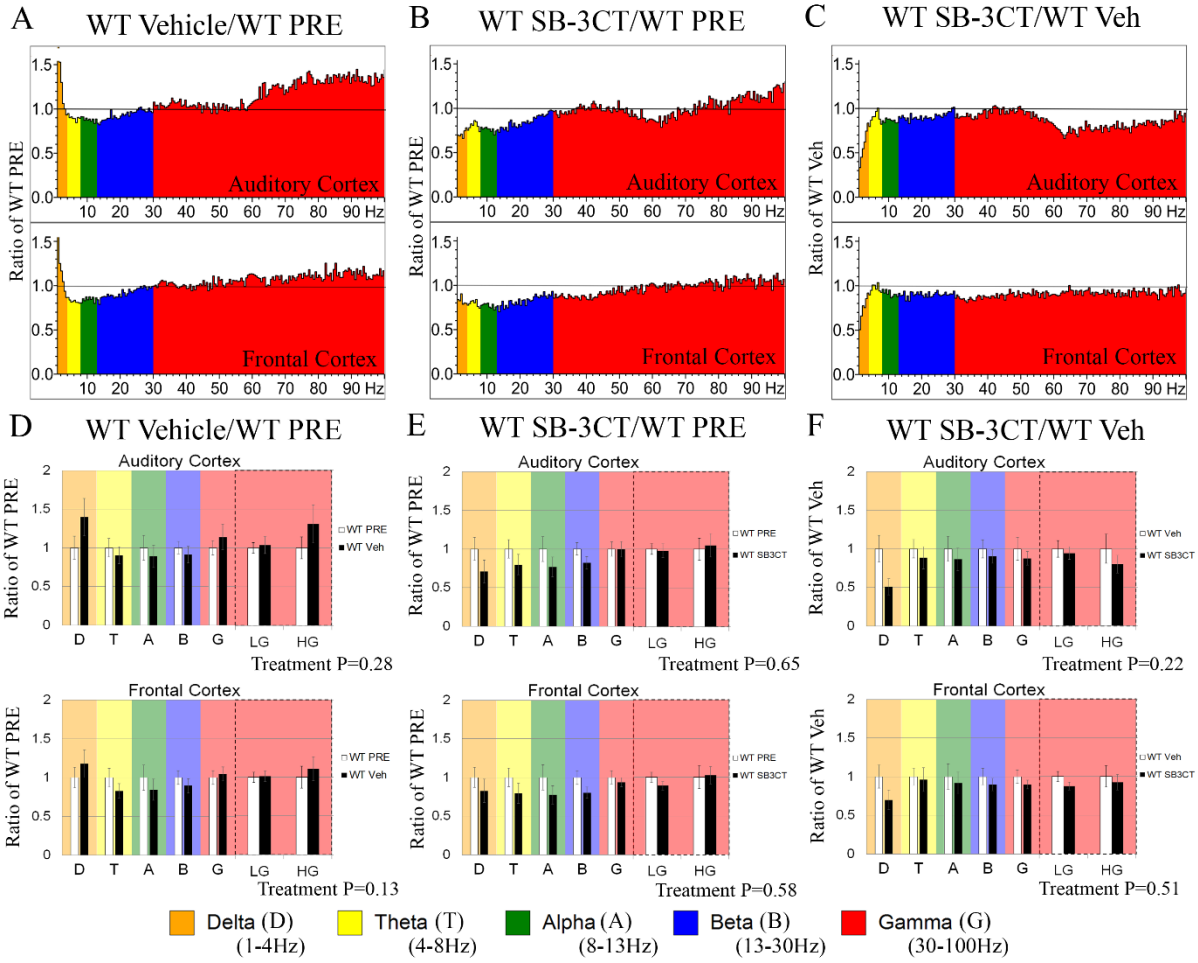

Supplemental Figure 2-5. Acute MMP-9 inhibition does not significantly alter resting gamma power in WT mice. Five minutes of resting EEG activity was recorded from electrodes implanted in the auditory (AC) and frontal cortex (FC) of WT and *Fmr1* KO mice. (A, B, D, E) Graphs show FFT calculated spectral power as a ratio of the WT control group (PRE, N=22) depicted in Figure 1. (A, D) Average power of vehicle-treated WT (N=16) mice in the AC (top) and FC (bottom). (B, E) Average power of SB-3CT-treated WT (N=15) mice. (C) Average power of SB-3CT-treated WT (N=15) mice compared to vehicle-treated WT (N=16) mice. One-way MANCOVA analysis of WT comparisons did not reveal any significant differences in any of the frequency bands in both the AC and FC. A value of 1 indicates no mean difference in power between WT treated and WT control, while values above the black line indicate WT treated > WT control, and below indicates WT treated < WT control.

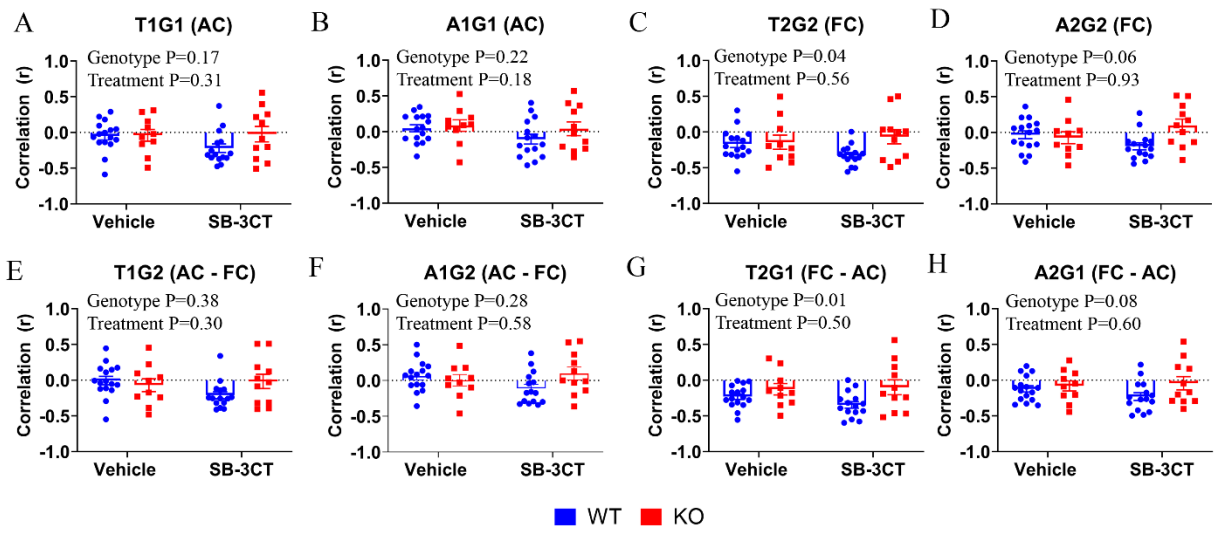

Supplemental Figure 2-6. Theta/LowGamma and Alpha/LowGamma EEG power coupling in AC and FC for treatment groups. (A-D) Graphs show the Theta/LowGamma (TG) and Alpha/LowGamma (AG) EEG power coupling for WT and *Fmr1* KO mice treated with vehicle or SB-3CT in the auditory cortex (represented by 1) and frontal cortex (represented by 2). (E-H) Graphs show cross EEG power coupling between the auditory cortex (1) and frontal cortex (2) for WT and *Fmr1* KO mice treated with vehicle or SB-3CT. Statistical analysis with two-way ANOVA for Theta/LowGamma and Alpha/LowGamma in the AC reveals no significant main effect of genotype (T1G1: F(1,48)=1.921, p=0.17; A1G1: F(1,48)=1.578, p=0.22), treatment (T1G1: F(1,48)=1.054, p=0.31: A1G1: F(1,48)=1.833, p=0.18) or interaction (T1G1: F(1,48)=1.58, p=0.21; A1G1: F(1,48)=0.53, p=0.47), respectively. Statistical analysis with two-way ANOVA for Theta/LowGamma in the FC reveals a significant main effect of genotype (T2G2: F(1,48)=4.104, p=0.04), but no significant main effect of treatment (T2G2: F(1,48)=0.353, p=0.56) or interaction (T2G2: F(1,48)=2.843, p=0.10). Statistical analysis with two-way ANOVA for Alpha/LowGamma in the FC revealed a significant interaction (A2G2: F(1,48)=5.997, p=0.02), but no main effect of genotype (A2G2: (F(1,48)=3.468, p=0.07) or main effect of treatment (A2G2: F(1,48)=0.008, p=0.93). Statistical analysis with two-way ANOVA for cross region Theta/LowGamma and Alpha/LowGamma coupling in the AC to FC reveals no significant main effect of genotype (T1G2: F(1,48)=0.777, p=0.38; A1G2: F(1,48)=1.21, p=0.28), treatment (T1G2: F(1,48)=1.11, p=0.30: A1G2: F(1,48)=0.31, p=0.58) or interaction (T1G2: F(1,48)=3.15, p=0.08; A1G2: F(1,48)=3.71, p=0.06), respectively. Statistical analysis with two-way ANOVA for cross region Theta/LowGamma coupling from FC to AC reveals a significant main effect of genotype (T2G1: F(1,48)=7.12, p=0.01), but no main effect of treatment (T2G1: F(1,48)=0.45, p=0.50) or interaction (T2G1: F(1,48)=1.19, p=0.28). Statistical analysis with two-way ANOVA for cross region Alpha/LowGamma coupling from FC to AC reveals no significant main effect of genotype (A2G1: F(1,48)=3.163, p=0.08), treatment (A2G1: F(1,48)=0.29, p=0.59), or interaction (A2G1: F(1,48)=1.30, p=0.26). For EEG power coupling comparisons, animals that moved less than five percent during the resting baseline were excluded from analysis (KO Veh N=2, KO SB N=1).

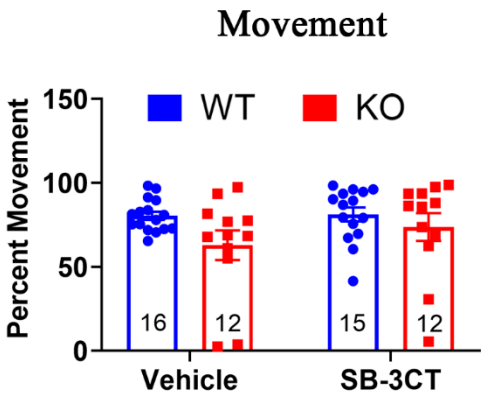

Supplemental Figure 2-7. Percent movement for vehicle-treated and SB-3CT WT and *Fmr1* KO mice. Graph shows percent movement during EEG resting baseline for WT and *Fmr1* KO mice following treatment. Statistical analysis of treatment groups with two-way ANOVA revealed a significant genotype effect ($F(1,51) = 4.46$, $p=0.04$), but no significant treatment ($F(1,91)=0.97$, $p=0.33$) or interaction effect ($F(1,51)=0.72$, $p=0.40$). *Post hoc* analysis with Bonferroni's multiple comparisons test did not reveal any significant differences between groups. For EEG power coupling comparisons, animals that moved less than five percent during the resting baseline were excluded from analysis (KO Veh N=2, KO SB N=1).

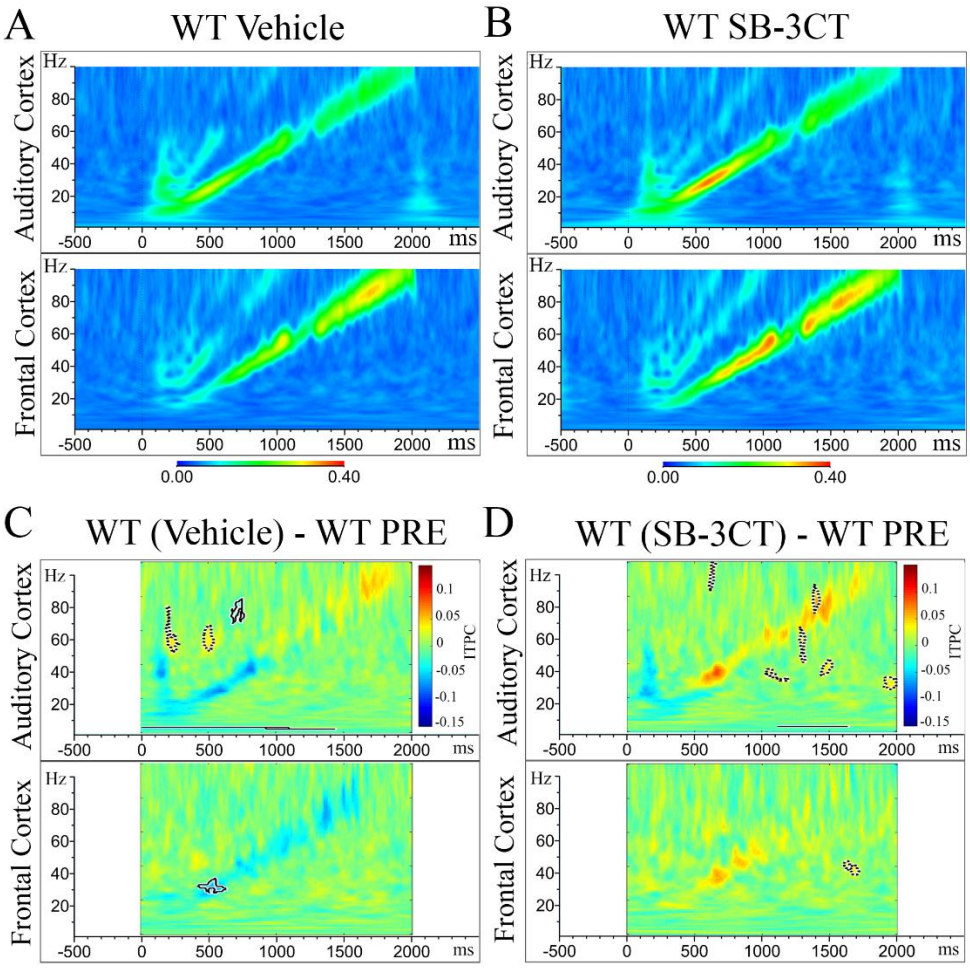

Supplemental Figure 4-1. Acute SB-3CT treatment does not significantly alter ITPC to auditory "Up Chirp" stimuli in WT mice. (A, B) Up chirp stimuli grand average ITPC in the AC (top) and FC (bottom) of vehicle-treated (N=17) and SB-3CT-treated (N=14) WT mice, respectively. Warmer colors, yellow/red, represent high ITPC values, while cooler colors, blue/green, represents low ITPC values. (C) Difference between vehicle-treated WT mice (N=17) and WT PRE (N=23) average chirp ITPC values in AC and FC. Blue areas indicate WT Veh <WT PRE, green areas represent no difference, and yellow areas WT Veh >WT PRE. (D) Difference between SB-3CT-treated WT (N=14) mice and WT PRE (N=23) average chirp ITPC values in AC and FC. For statistical analysis, clusters of p-values were calculated, and these differences were overlaid on the chirp response to demonstrate quantitative differences between each treatment group after correction for multiple comparisons. Using Monte Carlo statistical method on cluster analysis no significant differences were detected in AC or FC for average up chirp ITPC values between vehicle-treated WT (N=17) mice and WT PRE (N=23) mice (C). SB-3CT-treated WT (N=14) mice exhibited a significant increase in ITPC in high gamma band ITPC in the AC from 70-90Hz, but not FC compared to WT PRE (N=23) mice (D). Significantly different time x frequency bands between treatment groups are highlighted in bolded black lines. Similar patterns and statistics of ITPC were observed for both up and down chirps.

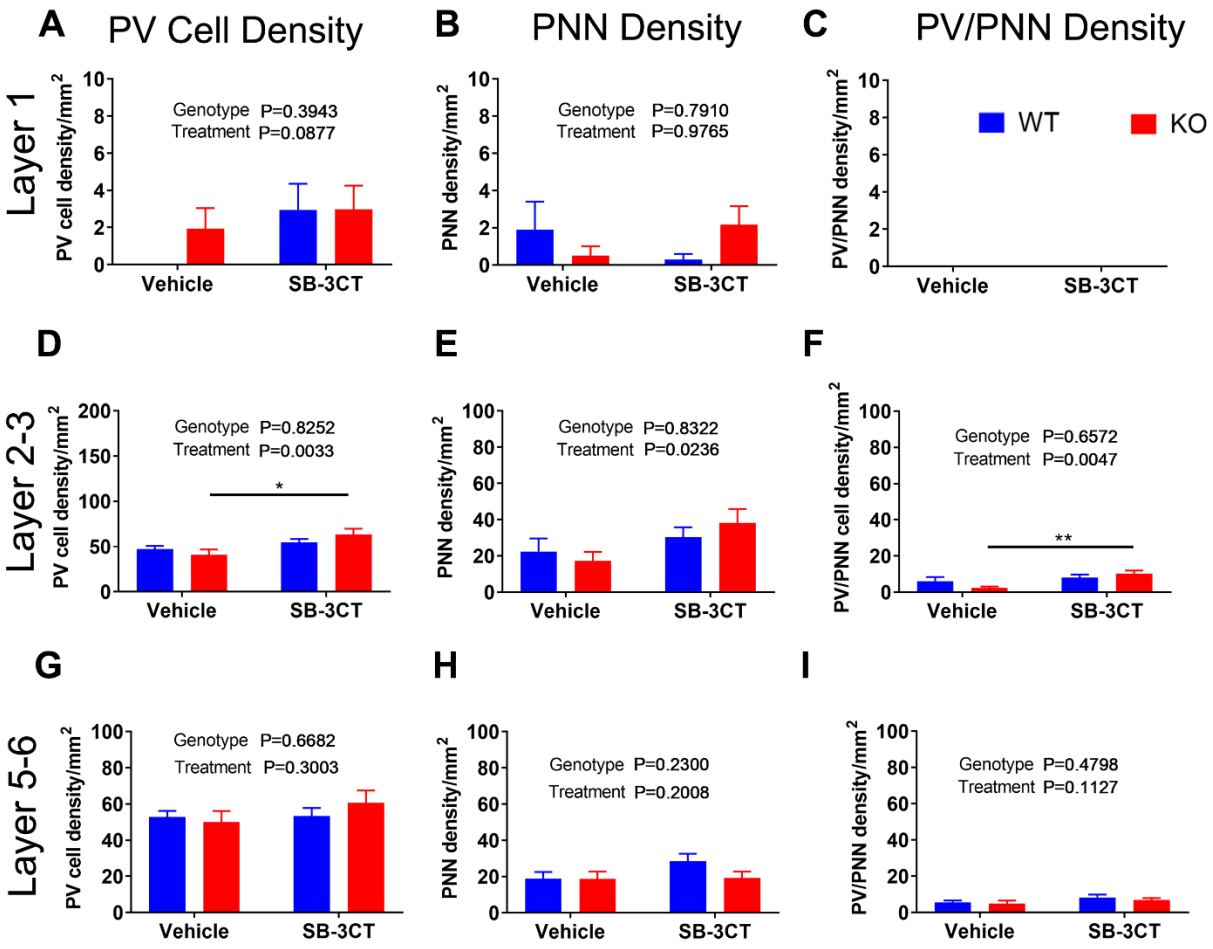

Supplemental Figure 5-1. PV/PNN quantification in auditory cortex. (A, D, G) Graphs show PV cell density in Layer 1, Layer 2-3, and Layer 5-6 of the auditory cortex. Statistical analysis reveals no significant differences in Layer 1. (B, E, H) Graphs show PNN density in Layer 1, Layer 2-3, and Layer 5-6 of the auditory cortex. Statistical analysis of PV, PNN density and PV/PNN colocalization in Layer 2-3 of the auditory cortex revealed a significant effect of treatment (PV: $F(1,74)=9.23$, $p=0.003$; PNN: $F(1,74)=5.34$, $p=0.02$; PV/PNN: $F(1,74)=8.50$, $p=0.005$), but no significant effect of genotype (PV: $F(1,74)=0.05$, $p=0.83$; PNN: $F(1,74)=0.05$, $p=0.83$; PV/PNN: $F(1,74)=0.20$, $p=0.66$) or interaction (PV: $F(1,74)=2.31$, $p=0.13$; PNN: $F(1,74)=1.08$, $p=0.30$; PV/PNN: $F(1,74)=3.18$, $p=0.08$). Statistical analysis of PV density and PV/PNN colocalization revealed a significant increase in SB-3CT-treated WT mice compared to vehicle-treated WT mice (Two-way ANOVA, $p=0.01$ (PV), $p=0.009$ (PV/PNN), $N=6$ per group). (C, F, I) Graphs show PV/PNN colocalization in Layer 1, Layer 2-3, and Layer 5-6 of the auditory cortex. Statistical analysis reveals no significant differences in Layer 5-6 of the auditory cortex. All graphs represent average values and the error bars indicate SEM.

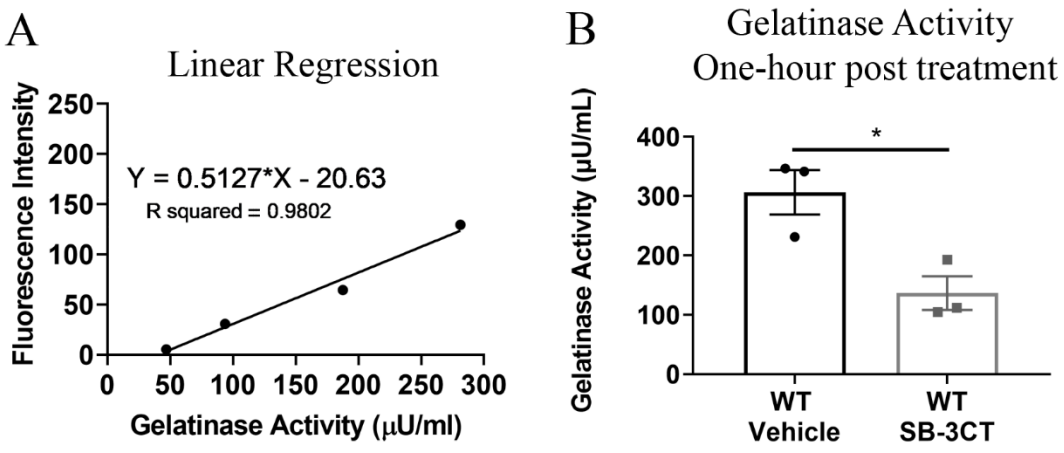

Supplemental Figure 7-1. SB-3CT inhibits gelatinase activity one-hour post treatment in WT mice. To confirm that the MMP-2/9 inhibitor, SB-3CT, reduced MMP-2/9 activity following treatment, gelatinase activity assay was measured using a Dye-Quenched gelatin assay. WT mice were injected intraperitoneally with SB-3CT (25 mg/kg) or vehicle and the auditory and surrounding cortices were collected and homogenized for the DQ gelatin assay one-hour post injection. (A) A mouse recombinant MMP-9 (specific activity approximately 1,500 pmol/min/μg) was used as a standard to obtain a readout of the approximate MMP-9 activity in the sample using a linear regression curve. (B) Graph show gelatinase activity in the cortices of vehicle-treated and SB-3CT-treated WT (C, N=3 per group, t-test, p=0.02) mice 1 h post injection.

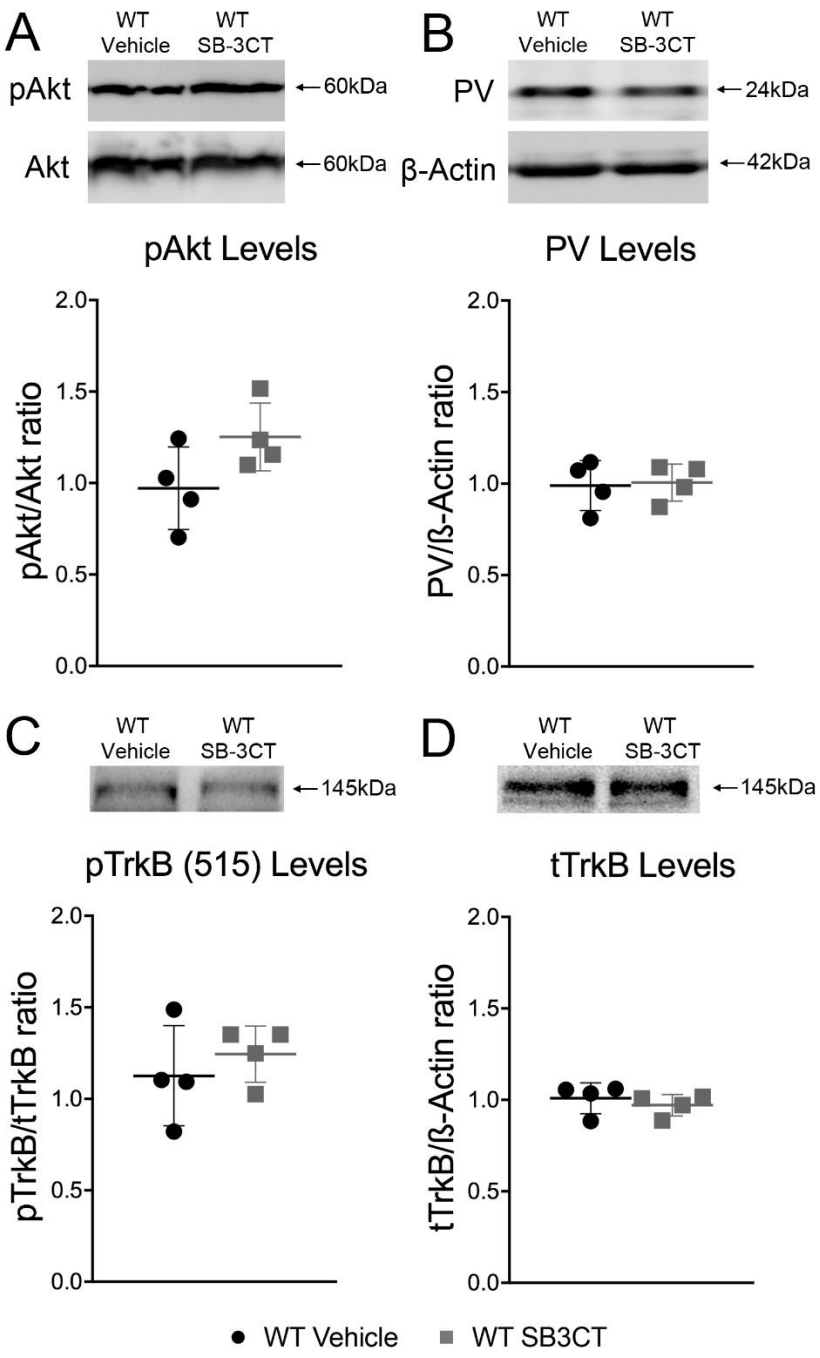

Supplemental Figure 7-2. Acute MMP-9 inhibition does not alter PV levels or phosphorylation of Akt/mTOR, and TrkB in the AC of WT mice. Western blots show levels of pAkt and Akt (A), PV and actin (B), pTrkB (Y515) (C) and total TrkB (D). Graphs show pAkt/Akt (A), PV/actin (B), pTrkB (Y515)/TrkB (C) and TrkB/actin (D) ratios in the auditory cortex of vehicle-treated and SB-3CT-treated WT mice (N=4 per group). All graphs represent average values and error bars indicate SEM.

Supplemental Table 1. Summary table of EEG resting baseline power ($\mu V^2/Hz$) for WT and *Fmr1* KO mice prior to treatment shown in Figure 1D (mean ± SEM).

Auditory Cortex (Figure 1F, top)

Genotype	Delta	Theta	Alpha	Beta	Gamma	Low Gamma	High Gamma
WT (N=22)	1.000 ± 0.149	1.000 ± 0.119	1.000 ± 0.161	1.000 ± 0.080	1.000 ± 0.094	1.000 ± 0.070	1.000 ± 0.140
KO (N=20)	1.043 ± 0.204	0.855 ± 0.125	0.788 ± 0.134	1.054 ± 0.109	1.306 ± 0.106	1.4154 ± 0.129 * (p=0.003)	1.145 ± 0.083

Frontal Cortex (Figure 1F, bottom)

Genotype	Delta	Theta	Alpha	Beta	Gamma	Low Gamma	High Gamma
WT (N=22)	1.000 ± 0.131	1.000 ± 0.120	1.000 ± 0.164	1.000 ± 0.088	1.000 ± 0.087	1.000 ± 0.063	1.000 ± 0.145
KO (N=20)	0.890 ± 0.163	0.716 ± 0.111	0.651 ± 0.107	0.925 ± 0.095	1.290 ± 0.100	1.328 ± 0.101 * (p=0.005)	1.210 ± 0.135

Auditory cortex (Figure 1G)

Genotype	**T1G1**	**A1G1**
WT (N=21)	**-0.214** ± 0.040	**-0.142** ± 0.042
***Fmr1* KO (N=18)**	**-0.052** ± 0.057 * (p=0.02)	**0.050** ± 0.056 ** (p=0.008)

Frontal Cortex (Figure 1H)

Genotype	**T2G2**	**A2G2**
WT (N=21)	**-0.290** ± 0.041	**-0.214** ± 0.045
***Fmr1* KO (N=18)**	**-0.146** ± 0.065, (p=0.06)	**-0.068** ± 0.063, (p=0.06)

Auditory to Frontal Cortex (Figure 1I)

Genotype	**T1G2**	**A1G2**
WT (N=21)	**-0.207** ± 0.044	**-0.130** ± 0.045
***Fmr1* KO (N=18)**	**-0.036** ± 0.061 * (p=0.03)	**0.016** ± 0.053 * (p=0.04)

Frontal to Auditory Cortex (Figure 1J)

Genotype	**T2G1**	**A2G1**
WT (N=21)	**-0.323** ± 0.032	**-0.261** ± 0.030

***Fmr1* KO (N=18)**	**-0.182** ± 0.061 * (p=0.04)	**-0.114** ± 0.063 * (p=0.03)

Supplemental Table 2. Summary table of EEG resting baseline power (μV^2/Hz) for WT and *Fmr1* KO mice post treatment with SB-3CT (25mg/kg) or vehicle shown in Figure 2D, 2E, 2F (mean ± SEM).

Auditory cortex (Figure 2D)

Genotype	Delta	Theta	Alpha	Beta	Gamma	Low Gamma	High Gamma
KO Vehicle (N=12)	0.567 ± 0.112	0.702 ± 0.147	0.761 ± 0.201	0.936 ± 0.140	1.371 ± 0.376	1.335 ± 0.273	1.406 ± 0.530
WT Vehicle (N=16)	1.000 ± 0.173	1.000 ± 0.120	1.000 ± 0.162	1.000 ± 0.116	1.000 ± 0.145	1.000 ± 0.107	1.000 ± 0.188

Frontal cortex

Genotype	Delta	Theta	Alpha	Beta	Gamma	Low Gamma	High Gamma
KO Vehicle (N=12)	0.698 ± 0.131	0.661 ± 0.129	0.637 ± 0.175	0.762 ± 0.087	1.088 ± 0.130	1.115 ± 0.125	1.018 ± 0.151
WT Vehicle (N=16)	1.000 ± 0.150	1.000 ± 0.112	1.000 ± 0.163	1.000 ± 0.104	1.000 ± 0.087	1.000 ± 0.064	1.000 ± 0.136

Auditory cortex (Figure 2E)

Genotype	Delta	Theta	Alpha	Beta	Gamma	Low Gamma	High Gamma
KO SB-3CT (N=12)	1.313 ± 0.262	1.043 ± 0.174	1.047 ± 0.120	1.135 ± 0.107	1.184 ± 0.110	1.194 ± 0.096	1.157 ± 0.166
WT SB-3CT (N=15)	1.000 ± 0.207	1.000 ± 0.164	1.000 ± 0.169	1.000 ± 0.098	1.000 ± 0.101	1.000 ± 0.090	1.000 ± 0.144

Frontal cortex

Genotype	Delta	Theta	Alpha	Beta	Gamma	Low Gamma	High Gamma
KO SB-3CT (N=12)	1.078 ± 0.198	0.889 ± 0.161	0.935 ± 0.172	1.053 ± 0.105	1.172 ± 0.149	1.20 ± 0.132	1.121 ± 0.202
WT SB-3CT (N=15)	1.000 ± 0.184	1.000 ± 0.160	1.000 ± 0.150	1.000 ± 0.092	1.000 ± 0.063	1.000 ± 0.059	1.000 ± 0.109

Auditory cortex (Figure 2F)

Genotype	Delta	Theta	Alpha	Beta	Gamma	Low Gamma	High Gamma
KO SB-3CT (N=12)	1.174 ± 0.234	1.312 ± 0.219	1.188 ± 0.215	1.094 ± 0.103	0.757 ± 0.070	0.845 ± 0.068	0.660 ± 0.095

KO Vehicle (N=12)	1.000 ± 0.120	1.000 ± 0.209	1.000 ± 0.264	1.000 ± 0.149	1.000 ± 0.275	1.000 ± 0.205	1.000 ± 0.377

Frontal cortex

Genotype	Delta	Theta	Alpha	Beta	Gamma	Low Gamma	High Gamma
KO SB-3CT (N=12)	1.081 ± 0.199	1.291 ± 0.234	1.350 ± 0.248	1.241 ± 0.124	0.966 ± 0.123	0.944 ± 0.104	1.018 ± 0.183
KO Vehicle (N=12)	1.000 ± 0.187	1.000 ± 0.195	1.000 ± 0.274	1.000 ± 0.114	1.000 ± 0.119	1.000 ± 0.113	1.000 ± 0.148

Supplemental Table 3. Summary table showing density of PV cells, WFA+ PNNs, PV/PNN co-localization, and PNN+/PV- cells in the layer 4 of the auditory cortex of WT and *Fmr1* KO mice post treatment with SB-3CT (25mg/kg) or vehicle shown in Figure 5 (mean ± SEM).

	WT Vehicle (n=18)	WT SB-3CT (n=23)	*Fmr1* KO Vehicle (n=20)	*Fmr1* KO SB-3CT (n=17)
PV+ cell density (N=6)	92.45 ± 4.60	103.09 ± 7.31 * (p=0.0215)	78.09 ± 5.11	99.05 ± 7.01
PNN+ density (N=6)	99.71 ± 11.16	142.50 ± 8.78 ** (p=0.0096), * (p=0.03)	64.15 ± 10.05 **** (p<0.0001)	104.74 ± 7.46 * (p=0.02)
PV+/PNN+ colocalization (N=6)	38.17 ± 4.10	56.17 ± 5.75 * (p=0.04)	27.51 ± 4.28 *** (p=0.0002)	50.55 ± 4.24 ** (p=0.009)
PNN+ / PV- (N=6)	61.53 ± 8.65	86.32 ± 7.18 **** (p<0.0001)	36.65 ± 6.36	54.19 ± 7.50 * (p=0.02)

Supplemental Table 4. Statistical results for Layer 4 auditory cortex PV/PNN analysis (Figure 5). All analysis was performed using two-way ANOVA.

	Genotype	Treatment	Interaction
PV+ cell density (N=6)	F(1,74) = 2.12, p=0.15	F(1,74) = 6.262, p=0.01	F(1,74)=0.67, p=0.42
PNN+ density (N=6)	F(1,74)=14.64, p=0.0003	F(1,74)=18.94, P<0.0001	F(1,74)=0.013, p=0.909
PV+/PNN+ colocalization (N=6)	F(1,74)=2.8, p=0.09	F(1,74)=17.78, p<0.0001	F(1,74)=0.268, p=0.606
PNN+ / PV- (N=6)	F(1,74)=14.53, p=0.0003	F(1,74)=8.00, p=0.006	F(1,74)=0.23, p=0.63

Supplemental Table 5. Summary table showing locomotor activity, anxiety, and hyperactivity measures for WT and *Fmr1* KO mice during elevated plus maze (EPM) and open field (OF) behavior tests shown in Figure 6A-H (mean ± SEM).

	WT Vehicle	WT SB-3CT	*Fmr1* KO Vehicle	*Fmr1* KO SB-3CT
Total Entries (EPM)	28.30 ± 2.86	31.38 ± 3.12	44.13 ± 3.01 **** (p<0.0001)	28.29 ± 2.97 ### (p=0.0001)
Speed (EPM)	26.04 ± 1.96	28.59 ± 2.14	33.64 ± 2.07 ** (p=0.003)	24.31 ± 2.04 ### (p=0.0008)
% Time in open arms (EPM)	69.50 ± 3.89	73.38 ± 4.25	43.13 ± 4.10 **** (p<0.0001)	72.79 ± 4.04 ####(p<0.0001)
Total line crosses (OF)	212.80 ± 15.40	232.30 ± 16.80	300.90 ± 16.20 **** (p<0.0001)	203.40 ± 16.00 ####(p<0.0001)
Speed (OF)	45.52 ± 3.73	50.98 ± 4.07	69.79 ± 3.93 **** (p<0.0001)	53.52 ± 3.87 ## (p=0.002)
Time spent in center/entry (OF)	0.93 ± 0.13	0.93 ± 0.14	0.52 ± 0.14 * (p=0.0173)	1.01 ± 0.13 ## (p=0.008)
% Time in thigmotaxis (OF)	47.79 ± 2.81	48.80 ± 3.06	68.04 ± 2.96 **** (p<0.0001)	50.21 ±2.92 ####(p<0.0001)
Center entries (OF)	6.00 ± 1.28	6.50 ± 1.40	2.30 ± 1.35 * (p=0.03)	7.00 ± 1.33 # (p=0.01)

Supplemental Table 6. Statistical results for locomotor activity, anxiety, and hyperactivity measures for WT and *Fmr1* KO mice during elevated plus maze (EPM) and open field (OF) behavior tests (Figure 6). All analysis was performed using two-way ANOVA.

	Genotype	Treatment	Interaction
Total Entries (EPM)	F(1,29) = 9.07, p=0.0053	F(1,29) = 9.11, p=0.0053	F(1,29) = 20, p=0.0001
Speed (EPM)	F(1,29) = 1.308, p=0.2620	F(1,29) = 5.452, p=0.0267	F(1,29) = 16.79, p=0.0003
% Time in open arms (EPM)	F(1,29) = 21.93, p<0.0001	F(1,29) = 33.92, p<0.0001	F(1,29) = 20.05, p=0.0001
Total line crosses (OF)	F(1,29) = 6.756, p=0.0145	F(1,29) = 11.71, p=0.0019	F(1,29) = 26.3, p<0.0001
Speed (OF)	F(1,29) = 26.33, p<0.0001	F(1,29) = 4.961, p=0.0341	F(1,29) = 17.71, p=0.0002
Time spent in center/entry (OF)	F(1,29) = 3.039, p=0.919	F(1,29) = 6.498, p=0.0163	F(1,29) = 6.533, p=0.0161
% Time in thigmotaxis (OF)	F(1,29) = 27.18, p<0.0001	F(1,29) = 16.38, p=0.0004	F(1,29) = 20.55, p<0.0001
Center entries (OF)	F(1,29) = 2.939, p=0.0972	F(1,29) = 7.668, p=0.0097	F(1,29) = 5.025, p=0.0328

Supplemental Table 7. Summary table showing gelatinase activity in the auditory cortex of WT and *Fmr1* KO mice one-hour post vehicle or SB-3CT (25mg/kg) treatment shown in Figure 7C (mean ± SEM).

	KO Vehicle	KO SB-3CT

Gelatinase Activity (µU/mL)	167.4 ± 23.69	33.87 ± 36.58 * (p=0.02)
	WT Vehicle	WT SB-3CT
Gelatinase Activity (µU/mL)	306.3 ± 37.64	136.4 ± 28.36 * (p=0.02)

Supplemental Table 8. Summary table showing protein levels in the auditory cortex of *Fmr1* KO mice one-hour post vehicle or SB-3CT (25mg/kg) treatment shown in Figure 7A-D (mean ± SEM).

	KO Vehicle (N=4)	KO SB-3CT (N=4)
PV levels	0.96 ± 0.07	1.44 ± 0.15 * (p-0.04)
p-Akt/Akt ratio	1.29 ± 0.08	0.76 ± 0.09 * (p=0.02)
p-TrkB(515)/TrkB ratio	1.00 ± 0.02	1.39 ± 0.12 * (p=0.03)
TrkB levels	1.00 ± 0.08	0.89 ± 0.06

Data Reporting Checklist

If any item is not applicable, indicate "n/a" ***and the reason why it is not applicable****!*

All information must be included in the manuscript.

Indicate the **page number** on which the respective information is provided.

Checklist item	Description	Page number
Ethical statement	• Confirm **institutional approval** and provide ethical approval **reference number.** **OR** • Confirm that institutional ethical approval was not required for your study in the methods section.	- 6 -
Study design	**Pre-registration** • Indicate if the study was **pre-registered.** Otherwise state in the manuscript that the study was not pre-registered. Preregistration usually encompasses official preregistration sites comparable to clinicaltrials.gov for clinical studies or https://osf.io/registries/. It means study protocols, endpoints and statistical analysis plans need to be (publicly) accessible. Checking and approval by the local ethics committee is not sufficient. **Randomization** • Describe the procedure of the **randomization method** (for e.g. simple randomization (which one?), block randomization, stratified randomization, or covariate adaptive randomization etc.) employed to allocate subjects to different experimental groups. Please be sure to describe the procedure *in detail* so that the reader can replicate the randomization methods easily. **OR** • If **no randomization** methods were used, then explicitly state in the manuscript "no randomization was performed to allocate subjects in the study". See this paper for a description with examples: (https://www.ncbi.nlm.nih.gov/pmc/articles/PMC3942596/) • Specify **the total number of animals used AND the initial number of animals used per group** in the materials and methods section. • Specify **order** in which animals were treated and assessed. **Blinding** • Describe blinding procedures for **each experiment** (who was blinded to which procedure during the study, i.e. the experimenter was unaware of the animal's group during experimentation, during (statistical) analysis, etc.). An experiment is also blind if the analysis or experimental group assignment is performed by a different person than the experimenter. **OR** • Explicitly state in the manuscript that **no blinding** was performed. **Predetermined sample size calculation** • Specify if **statistical methods** were employed to predetermine the **sample size** and include a description of sample size calculations (provide all parameters of the calculation and estimation of effect size) in the manuscript. **OR** • Explicitly state in the Methods section of the manuscript that **no sample calculation** was performed.	- 6 - - 14 - - 7/14 - 14 - 14-16, 18 - - 21 -

Checklist item	Description	Page number
	Outcomes • State pre-specified **primary or secondary endpoint**, otherwise state the study was exploratory.	-
	• Describe **inclusion and exclusion criteria** or state that no exclusion criteria were pre-determined.	- 11
	• State if any (and how many) **animals were excluded** based on the exclusion criteria or died during experiments.	- 7, 11, 14
	Time-line diagram or flow-chart (mandatory for animal studies) • Include in the Methods section a **graphical time-line or flow-chart** of the study design/ experimental procedure (including number of animals per group and number of excluded animals) and please provide a reference to the schematic in the manuscript text.	- 7 Supplemental Figure 1-1
	At the end of study report • Specify the **n number (n=)** in the figure legend and specify what it indicates (for e.g. n= number of independent cell culture preparations/ number of cells / number of animals / number of participants etc.).	-
	Avoid using the general term "**independent experiments**". Specify if you are referring to number of animals or independent cell culture preparations for example, i.e. how many independent cell preparations were used to achieve the n.	21
Experimental procedure	**Precise details of all procedures carried out:** • Include **Research Resource Identifiers (RRIDs)** (=> scicrunch.org) for all animals and relevant materials (chemicals, antibodies etc.) in the 'Methods' section. Make sure to always include the prefix RRID, otherwise, the reader will not know what to do with the reference and also add "RRID, Research Resource Identifier (see scicrunch.org)" to the abbreviation list.	- 6-21
	• When no RRID is available, provide **catalogue numbers**, including year of purchase, for all materials/equipment/kits/reagents used in the study.	- 6-21
	If you are using **custom-made materials**: ○ Please consider **obtaining an RRID number for your materials**. To do so, please create an account at https://www.scicrunch.org/resources . Then scroll down until you see the green bar that reads "Add a resource", click and follow the instructions.	- n/a did not use any custom made materials
	○ Include a statement indicating whether **custom-made materials** will be shared upon reasonable request.	-
	• State the **time of day at which the experiments** were conducted.	- 8, 18
	• Specify **anesthetic**.	- 7
	• Provide rationale for the choice of **anesthetic** used.	- 7
	• Describe how the animals were **killed**.	- 15

Checklist item	Description	Page number
	• Describe in detail what exact measures were taken to **minimize animal suffering after treatment/during experiments,** and please specify if and what type of medication was given to reduce animal pain during experiments. A general statement such as, "All efforts were made to minimize animal suffering" is not sufficient. One must provide a detailed description of these "methods".	- 7-8
Animals/ Cell lines	**Animals** • Indicate the **species**, **strain**, **sex**, **weight**, **age**, **housing** (cage type, number of cage companions) and **husbandry** (access to food and water) of animals in the Methods • Specify **original source** (company) of animals. **Cell lines** • State if the **cell line** is listed as a commonly misidentified cell line by the International Cell Line Authentication Committee (ICLAC; http://iclac.org/databases/cross-contaminations/). If the cell line is listed, provide a scientific justification to use this cell line • Indicate if, when and how **cell lines** were last authenticated (read: https://www.promega.de/resources/pubhub/cell-line-authentication-with-strs-2012-update/); • Indicate maximum number of **passages** for cell lines.	- 7 - 7 - n/a no cell lines were used - -
Reporting statistics	• Describe in a **separate section** what statistical analyses were carried out, their rationale, power analyses; • Specify the **statistical software** and version used to perform the statistical analyses; • Specify if an **assessment (and which one) of the normality of data** was carried out (an assessment of the normality of data is a prerequisite for many statistical tests because normal data is an underlying assumption in parametric testing); • Specify if a **test for outliers** (and which one) was conducted on the data and state if any data points were excluded; • **Show individual data points** (mandatory for small sample sizes n<15) as a dot-plot or use box-plots instead of simple bar graphs. More information as to why this is important can be found here: https://journals.plos.org/plosbiology/article?id=10.1371/journal.pbio.1002128	- 20-21 - 13,18-20 - 10-11, 22 - 10-11 - Figures 1, 5, 6 and 7